The Horizontal Kinetic Energy Spectrum and Spectral Budget Simulated by a High-Resolution Troposphere–Stratosphere–Mesosphere GCM

JOHN N. KOSHYK

Department of Physics, University of Toronto, Toronto, Ontario, Canada

KEVIN HAMILTON

NOAA/Geophysical Fluid Dynamics Laboratory, Princeton, New Jersey

(Manuscript received 10 December 1999, in final form 12 May 2000)

ABSTRACT

Horizontal kinetic energy spectra simulated by high-resolution versions of the Geophysical Fluid Dynamics Laboratory SKYHI middle-atmosphere general circulation model are examined. The model versions considered resolve heights between the ground and ~80 km, and the horizontal grid spacing of the highest-resolution version is about 35 km. Tropospheric kinetic energy spectra show the familiar ~ -3 power-law dependence on horizontal wavenumber for wavelengths between about 5000 and 500 km and have a slope of $\sim -5/3$ at smaller wavelengths. Qualitatively similar behavior is seen in the stratosphere and mesosphere, but the wavelength marking the transition to the shallow regime increases with height, taking a value of ~2000 km in the stratosphere and ~4000 km in the mesosphere.

The global spectral kinetic energy budget for various height ranges is computed as a function of total horizontal wavenumber. Contributions to the kinetic energy tendency from nonlinear advective processes, from conversion of available potential energy, from mechanical fluxes through the horizontal boundaries of the region, and from parameterized subgrid-scale dissipation are all examined. In the troposphere, advective contributions are negative at large scales and positive over the rest of the spectrum. This is consistent with a predominantly downscale nonlinear cascade of kinetic energy into the mesoscale. The global kinetic energy budget in the middle atmosphere differs significantly from that in the troposphere, with the positive contributions at most scales coming predominantly from vertical energy fluxes.

The kinetic energy spectra calculated from two model versions with different horizontal resolution are compared. Differences between the spectra over the resolved range of the lower-resolution version are smallest in the troposphere and increase with height, owing mainly to large differences in the divergent components. The result suggests that the parameterization of dynamical subgrid-scale processes in middle-atmosphere general circulation models, as well as in high-resolution tropospheric general circulation models, may need to be critically reevaluated.

1. Introduction

The large-scale tropospheric kinetic energy (KE) spectrum as a function of horizontal wavenumber and the physical processes maintaining it have been studied for almost half a century (e.g., Charney 1947; Smagorinsky 1953; Saltzman and Teweles 1964). The standard view (e.g., Lorenz 1967) begins with generation of zonal available potential energy by the meridional gradient of solar heating. This is converted by baroclinic instability into eddy available potential energy and eddy KE, principally in zonal wavenumbers ~2–10. Nonlinear interactions transfer the eddy KE mainly upscale from the generation scales to zonal wavenumbers 1 and 0 (the zonal mean), although some energy is transferred downscale.

The theory of isotropic inertial range turbulence provides a useful conceptual framework for understanding the observed tropospheric KE spectrum. The theory is based on a system with eddy forcing concentrated in a narrow band of spectral wavenumber space and eddy dissipation acting only at large wavenumbers, well separated from the forcing scales. For the case of purely horizontal flow, the turbulent transfer of energy among the different spatial scales was discussed by Fjørtoft (1953). He noted that the constraint of enstrophy conservation inhibits downscale KE transfer in 2D flow, in contrast to the 3D case (Kolmogorov 1941). Kraichnan (1967) derived the 2D analog of Kolmogorov's 3D inertial range results. In terms of the horizontal wavenumber, k_H, Kraichnan's theory predicts a $k_H^{-5/3}$ inertial

Corresponding author address: Dr. John Koshyk, Department of Physics, University of Toronto, Toronto, ON M5S 1A7, Canada.
E-mail: koshyk@mam.physics.utoronto.ca

range for wavenumbers $k_H < k_F$, where k_F represents the forced scale, and a k_H^{-3} inertial range for $k_H > k_F$. In the idealized limit of infinite Reynolds number the k_H^{-3} inertial range is characterized by a downscale enstrophy cascade and no energy cascade, and the $k_H^{-5/3}$ inertial range by upscale energy cascade and no enstrophy cascade. Kraichnan's predictions for the power-law spectra were largely confirmed in 2D numerical simulations by Lilly (1969). Charney (1971) generalized Kraichnan's results, showing that they are also predicted by quasigeostrophic theory.

These theoretical and idealized modeling studies were restricted to unbounded systems on a uniformly rotating plane. Baer (1972) and Tang and Orszag (1978) considered the generalization of KE spectra to spherical geometry. Boer and Shepherd (1983) used global meteorological analyses to calculate the monthly mean horizontal KE spectrum as a function of total horizontal wavenumber, n. They found that the KE behaves as $\sim n^{-3}$ and that enstrophy cascades downscale for the range of n corresponding to horizontal wavelengths between ~1000 and 5000 km, consistent with the predictions of 2D and quasigeostrophic turbulence theories, with the source for the eddy motions concentrated near scales of ~5000 km ($n \sim 8$). For $n \lesssim 8$, Boer and Shepherd found no clear power-law behavior.

For horizontal wavelengths smaller than ~1000 km, it is difficult to employ global meteorological analyses to reliably determine the KE spectrum, but other observations show that the n^{-3} power law does not hold throughout this wavelength regime. Perhaps the best evidence for this is provided by detailed observations of the winds in the upper troposphere from instrumented commercial aircraft as analyzed by Nastrom et al. (1984) and Nastrom and Gage (1985). They plotted horizontal wavenumber spectra of the zonal wind, u, and meridional wind, v, covering the wavelength range ~10–10 000 km, and found a $\sim k_H^{-3}$ regime at long wavelengths, with a fairly well defined break at wavelengths of ~500 km, to a $\sim k_H^{-5/3}$ regime at smaller scales. Cho et al. (1999a,b) analyzed some more recent aircraft data collected above the Pacific Ocean and also found that KE spectra follow a $\sim k_H^{-5/3}$ power law at mesoscales.

While there is reasonably convincing theory for the k_H^{-3} regime at large scales, the explanation for the shallow $\sim k_H^{-5/3}$ spectrum in the mesoscale is more controversial. VanZandt (1982) suggested that motions in this regime contain a significant component from free internal gravity waves. Results from various simplified models that allow divergent motions show that the mesoscale regime is characterized by a dominant downscale KE cascade of rotational modes combined with direct, spontaneous generation of gravity waves (Farge and Sadourny 1989; Polvani et al. 1994; Yuan and Hamilton 1994; Bartello 1995). Yuan and Hamilton (1994) examined the statistical equilibrium in an f-plane, shallow-water model randomly forced within a narrow band of small wavenumbers, and with dissipation at very small scales provided by a hyperviscosity. The results showed a ~ -3 spectral slope for KE at scales smaller than the forcing scales, extending to a transition wavenumber, $k_* \sim f/U$, where f is the Coriolis parameter and U is a typical value of horizontal velocity. (Note that the Rossby number $R_o = 1$ at $k = k_*$.) For $k_H > k_*$ the spectral slope was shallower than -3. Yuan and Hamilton divided the flow into a balanced component, characterized by a purely diagnostic relation between pressure and wind, and a residual that had properties much like linear inertio-gravity waves. The balanced component had a spectrum close to k_H^{-3} for all k_H and the residual was much flatter, accounting for the shallowing of the total KE spectrum for $k_H > k_*$.

A competing explanation for the observed $k_H^{-5/3}$ power-law regime is provided by the theory of quasi-2D turbulence. Within this framework, the $k_H^{-5/3}$ regime is seen as an inertial subrange with a quasi-horizontal upscale KE cascade from an energy source at relatively small scales, presumably associated with moist convection (Lilly 1983; Gage and Nastrom 1986; Vallis et al. 1997). The Froude number in this theory is assumed to be small and the flow is essentially balanced.

While idealized model studies show that both the quasi-2D (balanced) and the gravity wave (unbalanced) mechanisms underlying the $k_H^{-5/3}$ regime are plausible, the explanation for the mesoscale regime in the real troposphere remains unclear.

In the middle atmosphere, the relevance of inertial range turbulence theories is not at all obvious. In particular, it is believed that the major input to middle-atmospheric eddy energy is the upward flux from waves forced in the troposphere. This upward flux occurs on a range of space- and timescales, from planetary scales (e.g., Charney and Drazin 1961) to small-scale, high-frequency motions thought to be associated with vertically propagating gravity waves (e.g., Hines 1960). While the significance of vertical wave propagation for the eddy motions in the middle atmosphere is generally acknowledged, the relative roles of vertical fluxes versus quasi-horizontal energy cascades are not well understood. [See O'Neill and Pope (1988) and Scinocca and Haynes (1998) for studies related to this issue.] A thorough quantitative understanding of the mechanisms maintaining the KE spectrum in either the troposphere or the middle atmosphere has not been achieved, despite the important work on theory and idealized models mentioned above.

A plausible approach to understanding the maintenance of the KE spectrum in the atmosphere is detailed diagnostic analyses of comprehensive global general circulation models (GCMs). While such models have important limitations, they do include self-consistent representations of all the significant processes involved in KE generation, transfer, and dissipation. The model results can, in principle, also be diagnosed exactly, unlike the imperfectly sampled real atmosphere.

The horizontal KE spectrum simulated by tropospher-

ic GCMs has been examined in a number of earlier studies (Charney 1971; Boer et al. 1984; Koshyk and Boer 1995; Koshyk et al. 1999b). Koshyk et al. (1999a) compared the KE spectrum as a function of height in five different middle-atmosphere models. GCMs have successfully produced a realistic n^{-3} regime in the troposphere, but have generally been run at too coarse spatial resolution to allow simulation of the tropospheric mesoscale regime. The present paper discusses the KE spectra simulated by very high horizontal resolution versions of a comprehensive middle-atmosphere GCM resolving a broad portion of the tropospheric mesoscale. The model considered extends from the ground to the mesopause. The focus is on understanding the behavior of the spectrum as a function of height and on detailed diagnosis of the spectral energy budgets. A preliminary report on some of the tropospheric results presented here has appeared in Koshyk et al. (1999b).

The models analyzed in this study are described in section 2. In section 3, simulated one-dimensional horizontal wavenumber spectra are discussed and compared with available observations. Section 4 consists of a spherical harmonic analysis of model data in the troposphere, where KE spectra are computed as functions of the total horizontal wavenumber *n*. Spectral KE budgets associated with the spectra in section 4 are presented in section 5, and the contributions to the spectra from different latitude bands are discussed in section 6. Spectra and spectral budgets for the stratosphere and mesosphere are analyzed in section 7, and the conclusions are summarized in section 8.

2. Model description

The model employed for the present calculations is the Geophysical Fluid Dynamics Laboratory (GFDL) SKYHI GCM (Fels et al. 1980; Hamilton et al. 1995), which solves the governing equations discretized on a global latitude–longitude grid. Earlier publications have examined results from model simulations at various spatial resolutions (e.g., Hamilton et al. 1995; Jones et al. 1997). In this paper some unprecedentedly high-resolution results are described from versions of the model with $1^\circ \times 1.2^\circ$ and $0.33^\circ \times 0.4^\circ$ latitude–longitude grids (referred to as N90 and N270 respectively, where the notation indicates the number of latitude rows in one hemisphere), and either 40 (''L40'') or 80 (''L80'') levels in the vertical between the ground and 0.0096 mb (~80 km). The level spacing is smallest near the ground and increases with height, so that the L40 and L80 models contain 15 and 30 levels, respectively, between the ground and 100 mb (~17 km). The vertical coordinate surfaces are terrain-following at the ground and deform smoothly to purely isobaric surfaces above 353 mb. Results from integrations of the N90L40, N90L80, and N270L40 versions of the model are analyzed. The basic climatology of these runs is described in Hamilton et al. (1999). Also of relevance to this study is the work of Strahan and Mahlman (1994a,b), who performed a spectral analysis of passive tracers in the N90L40 model version.

The model includes a sophisticated treatment of radiative transfer with prescribed cloud amounts, realistic topography and seasonally varying sea surface temperatures, a parameterized hydrological cycle including soil moisture storage, and a parameterization of stable precipitation. Moist convective adjustment is performed at each time step. In common with other GCMs, the SKYHI model includes a parameterization of the effects of subgrid-scale motions in the horizontal momentum and thermodynamic equations that is formulated as a local diffusive mixing.

The vertical momentum mixing is treated as a second-order diffusion with coefficient, K_V, that varies as a function of the model level spacing and the local Richardson number, Ri of the resolved flow (see Levy et al. 1982).

The horizontal subgrid-scale mixing is the nonlinear eddy viscosity scheme of Smagorinsky (1963), modified by Andrews et al. (1983). The nonlinear diffusion coefficient is given by

$$K_H = (k_o \Delta y)^2 |D|, \tag{1}$$

where $k_o = 0.1$ is a dimensionless constant, Δy is the horizontal grid spacing, and $|D|$ is related to the local horizontal flow deformation and strain fields.

The models used here contain no parameterization of subgrid-scale gravity wave momentum fluxes. However, gravity waves in the model are spontaneously generated by a variety of mechanisms including flow over topography and moist convection. The moist convection contribution to the middle-atmospheric gravity wave field has been characterized in lower-resolution versions of the model, and shown to be very important (Manzini and Hamilton 1993). Time stepping is explicit, trading computational expense for numerical accuracy in the representation of gravity wave motions; spatial derivatives are approximated by second-order centered differences.

The present paper examines data from a single July of a simulation with the N270L40 model. Results are compared to those from July simulations with the N90L40 and the N90L80 models. Details of the initialization of the simulations are given in Hamilton et al. (1999). Results for January are qualitatively similar to those presented here for July, and this is discussed further in section 8.

3. One-dimensional Fourier spectra

The main focus of this paper is on the characterization of model results in terms of two-dimensional horizontal spectra. However, as noted earlier, there are no reliable observational data to allow computation of global two-dimensional spectra at mesoscales. Thus, detailed comparisons with observations for the mesoscale can be

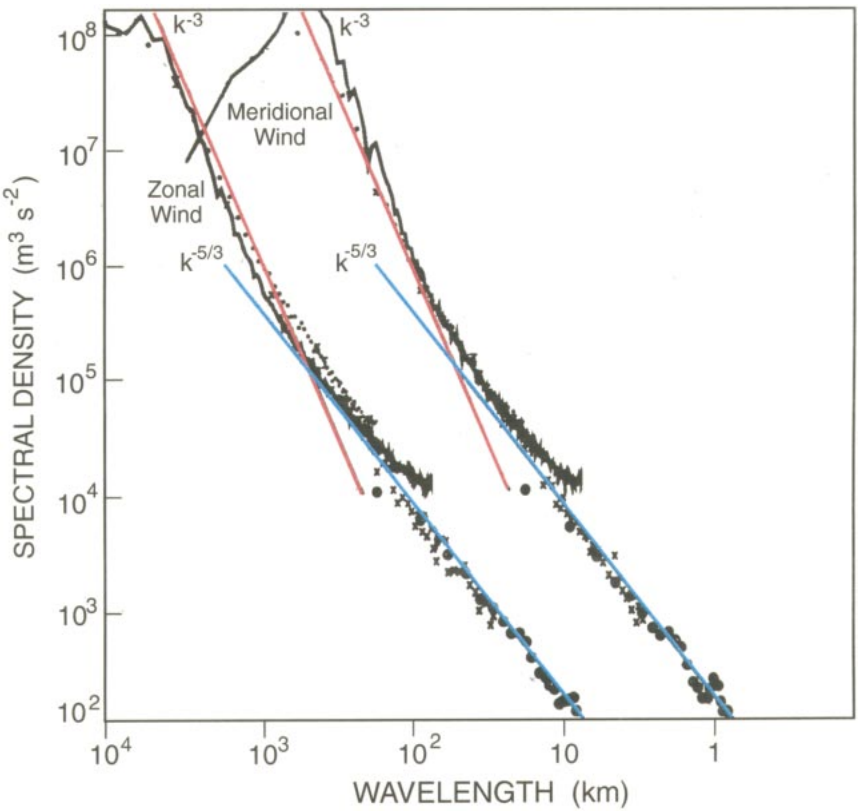

FIG. 1. Zonal wavenumber spectra of the zonal and meridional wind components in the upper troposphere. The data points are reproduced from Nastrom et al. (1984) and show actual observations based on data from commercial aircraft flights, with different symbols representing results obtained using different lengths of flight segments. The straight lines are drawn for reference and have slopes of $-5/3$ and -3. The solid curve is for the N270L40 SKYHI model along the 45°N latitude circle and at 211 mb, monthly averaged for a single Jul. For clarity the results for the meridional wind have been shifted one decade to the right.

based only on one-dimensional sections through the atmosphere.

Nastrom et al. (1984), Nastrom and Gage (1985), and Gage and Nastrom (1986) computed horizontal kinetic energy spectra over a wide range of scales, including the mesoscale, using data from the Global Atmospheric Sampling Program (GASP) during 1975–79. The data include measurements of in situ winds and temperatures taken on almost 7000 predominantly east–west flights of instrumented commercial airliners. Approximately 80% of the flight segments were confined between 35° and 55°N, although data from some flights in the Tropics and Southern Hemisphere were also obtained. The great bulk of the flight paths lie in the upper troposphere, typically between 150 and 350 mb. The individual points in Fig. 1 reproduce results of the Nastrom et al. (1984) analysis of GASP data. Variance spectra of u and v as a function of k_H are shown. The distinct steep large-scale and shallow mesoscale regimes are evident. The solid curves show comparable results for the N270L40 SKYHI simulation. Model zonal wavenumber spectra of u and v at 211 mb around the 45°N latitude circle, averaged over 1488 half-hourly snapshots during July, are plotted. There is generally good agreement between the simulation and the GASP data, and, in particular, the model displays a clear shallow regime at wavelengths less than 500 km. The model and observations disagree over the wavelength range ~140–70 km, with the model spectra shallower than observed. This ''bending up'' of the spectrum near the smallest resolved scales may be an indication of insufficient subgrid-scale dissipation in the model. However, the model is able to resolve a significant portion of the shallow mesoscale regime, so the transition to the mesoscale near wavelengths of about 500 km is well separated from the possibly unphysical behavior near the spectral tail.

The model results of Fig. 1 are supplemented in Fig. 2 by zonal wavenumber spectra at the equator and at 45°S. Spectra are shown for both 211 and 0.13 mb (~65 km). The results for 211 mb are similar at 45°N and 45°S. At both latitudes there is somewhat more power in v than in u over the wavelength range 10 000–1000

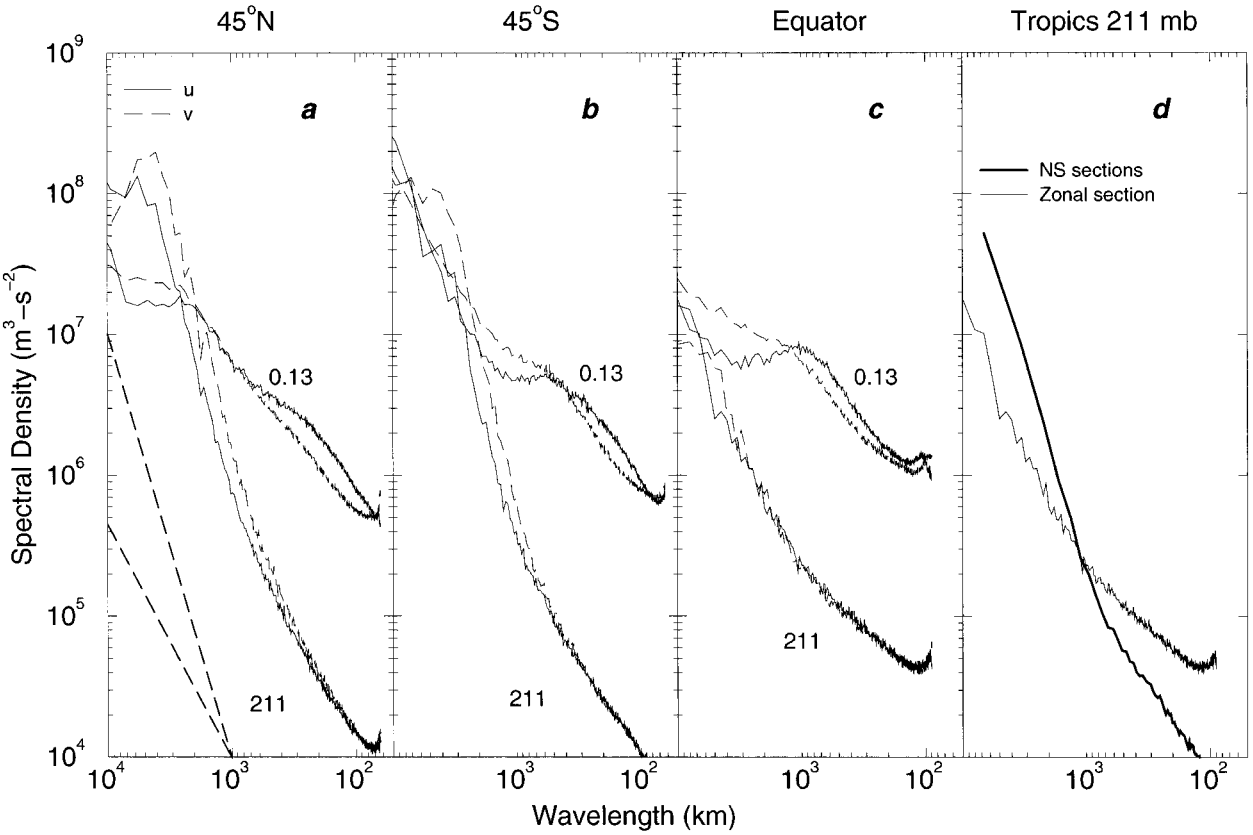

FIG. 2. N270L40 Jul mean zonal wavenumber spectra at (a) 45°N, (b) 45°S, and (c) 0°. Zonal and meridional velocity variance spectra are shown at the 211- and 0.13-mb levels in each panel. The curves in (a) at 211 mb are identical to the curves in Fig. 1. The 211-mb variance spectrum of zonal velocity at the equator in (c) is reproduced in (d), together with its meridional wavenumber spectrum computed from data along several north–south sections between 30°N and 30°S. The meridional wavenumber spectra are averaged to produce the single north–south curve in (d). The dashed curves in (a) are for reference and have slopes of $-5/3$ and -3.

km, and there is near equipartition of u and v spectral variance at wavelengths smaller than about 1000 km.

The 211-mb equatorial spectrum differs from those at 45°N and 45°S in having much more variance in the mesoscale and much less at large scales. The tendency for the eddy activity in SKYHI to be enhanced near the equator has been noted in earlier studies characterizing vertical gravity wave fluxes into the middle atmosphere (Hayashi et al. 1989; Manzini and Hamilton 1993). Nastrom and Gage (1985) computed KE spectra from the rather limited number of GASP flight segments in the Tropics. They concluded that the spectrum in the Tropics is similar to that in midlatitudes, and their results show no evidence for the enhancement of equatorial KE displayed in the model results of Fig. 2. One difference between the present equatorial analysis of the model simulation and the GASP data is that the tropical segments used by Nastrom and Gage were primarily cross-equatorial flights, aligned very roughly north–south (many on flights between Australia and Northern Hemisphere locations). Figure 2d compares the equatorial u variance spectrum at 211 mb reproduced from Fig. 2c with the u spectrum averaged over north–south samples (spanning 30°N–30°S) in the model. There is a major difference between the spectra based on the ''tropical'' north–south slice and the equatorial zonal slice. This difference is probably ascribable to a combination of significant anisotropy (i.e., different eddy variances in the zonal and meridional directions, at least in the Tropics) and geographical variability (e.g., concentration of variance right near the equator). Both of these aspects have analogs in the two-dimensional KE spectra discussed in sections 4 and 6. The north–south section results in Fig. 2d are actually quite similar to the 45°N and 45°S zonal spectra, and are in reasonable agreement with the GASP tropical spectra shown in Nastrom and Gage (1985).

The 0.13-mb spectra in Fig. 2 are shallower than those at 211 mb at all latitudes. The tendency for the zonal KE spectrum to become shallower with height has been seen in earlier SKYHI studies (Hamilton 1993). For vertically propagating gravity waves the vertical group velocity is proportional to k_H, so that waves with large k_H can preferentially survive dissipative processes, and should increasingly dominate the spectrum at higher altitudes. The only comparable observations that exist are

determinations of the density fluctuations along quasi-horizontal paths during National Aeronautics and Space Administration space shuttle reentries. Fritts et al. (1989) computed density spectra spanning wavelengths of about 20–4000 km for several reentries in the altitude range of 60–90 km, and generally found fairly shallow power-law spectra (slopes between -1 and -2) for wavelengths less than about 2000 km. The experience from the GASP data suggests that the horizontal velocity spectrum and the density spectrum should have similar shapes. If this is also the case in the mesosphere, then the Fritts et al. data are consistent with the 0.13-mb model spectra in Fig. 2.

4. Two-dimensional spherical harmonic spectra in the troposphere

a. Computation of the spherical harmonic spectra

The KE spectrum can be calculated as a function of the total spherical harmonic wavenumber by expanding the horizontal velocity components in a triangularly truncated series of spherical harmonics (Baer 1972):

$$u(\lambda, \phi, p, t) = \sum_{n=0}^{N} \sum_{m=-n}^{n} u_{n,m}(p, t) P_{n,m}(\cos\phi) e^{im\lambda}$$

$$v(\lambda, \phi, p, t) = \sum_{n=0}^{N} \sum_{m=-n}^{n} v_{n,m}(p, t) P_{n,m}(\cos\phi) e^{im\lambda}, \quad (2)$$

where m and n are the zonal and total wavenumbers, N is the truncation wavenumber, and $P_{n,m}$ is the Legendre polynomial of degree n. The spherical harmonics, $Y_{n,m} = P_{n,m} e^{im\lambda}$, form an orthogonal set of basis functions on the sphere; some of their properties are given in Boer (1983). The spectrum of KE per unit mass follows from the spectral coefficients for u and v as

$$E_{n,m}(p, t) = (|u_{n,m}(p, t)|^2 + |v_{n,m}(p, t)|^2)/4. \quad (3)$$

An alternative expression for the KE spectrum is obtained by partitioning the horizontal velocity field into its rotational and divergent parts as follows:

$$\mathbf{v} = (u, v) = \mathbf{k} \times \nabla\psi + \nabla\chi, \quad (4)$$

where ψ is the streamfunction and χ is the velocity potential. Expanding ψ and χ in spherical harmonic series, and noting that the vorticity $\zeta = \nabla^2\psi$ and the divergence $\delta = \nabla^2\chi$, the KE spectrum per unit mass, $\mathcal{E}_{n,m}(p, t)$, can be written

$$\mathcal{E}_{n,m}(p, t) = \frac{1}{4} \frac{a^2}{[n(n+1)]} (|\zeta_{n,m}(p, t)|^2 + |\delta_{n,m}(p, t)|^2), \quad (5)$$

where a is the earth's radius (Lambert 1984). Differences between the expressions for KE in (3) and (5) are discussed in the appendix and are minimal beyond the largest decade of spatial scales. Spectra based on (3) and (5) have also been compared in Boer and Shepherd (1983) using FGGE-IIIb data.

Spectra are computed from 12-hourly snapshots of the model velocity fields on pressure levels. (i.e., exactly on model isobaric levels for $p < 353$ mb, and using data interpolated to pressure levels closely corresponding to model levels for $p > 353$ mb). In order to project the fields onto spherical harmonics, the data are interpolated from the model latitude–longitude grid to a Gaussian grid. For the N270L40 version the grid used is that appropriate for an expansion with $N = 450$, or T450 truncation, in standard meteorological notation. For the N90 version, T150 truncation is used. Results are vertically integrated over four regions of the atmosphere, loosely referred to here as the lower troposphere (291–893 mb), the upper troposphere (92–353 mb), the stratosphere (0.91–149 mb), and the mesosphere (0–1.28 mb). The lower bound for the lower troposphere is chosen in order to minimize the effects of interpolation below the ground while simultaneously retaining a reasonable sampling of the lowermost troposphere. The vertical boundaries chosen correspond exactly to model half levels, and the vertical overlap between altitude regions arises because each adjacent pair of regions contains one common full level.

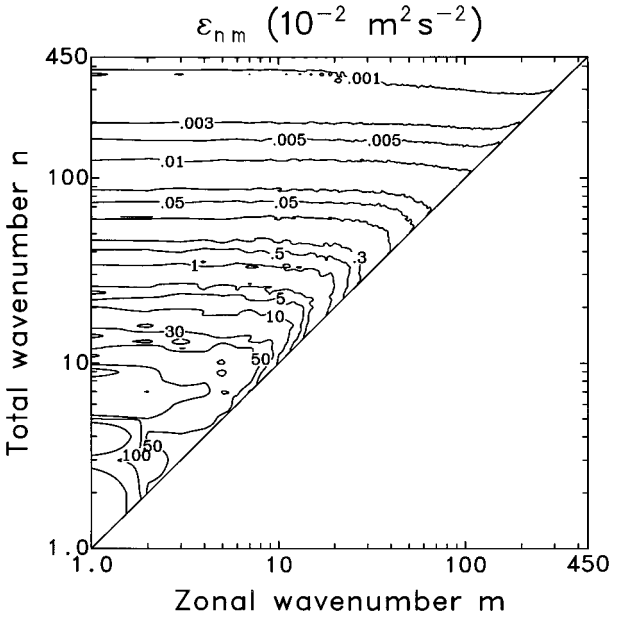

FIG. 3. N270L40 Jul mean KE spectrum vertically averaged over the 92–353-mb layer. The spectrum, $\mathcal{E}_{n,m}$, is shown as a function of zonal wavenumber m and total wavenumber n. The nondimensional value $n = 1$ corresponds to a wavelength of approximately 40 000 km. Contour values are 0.001, 0.003, 0.005, 0.01, 0.03, 0.05, . . . $\times 10^{-2}$ m^2 s^{-2}.

The field $\mathcal{E}_{n,m}$, temporally averaged over a single July and vertically integrated over the upper troposphere, is shown in Fig. 3. The nondimensional value $n = 1$ corresponds to a wavelength of approximately 40 000 km. The spectrum shows only a very weak dependence on m for all wavenumbers $n \gtrsim 100$, suggesting that the flow is essentially isotropic at these length scales. For scales $10 \lesssim n \lesssim 100$, the spectrum depends on m for

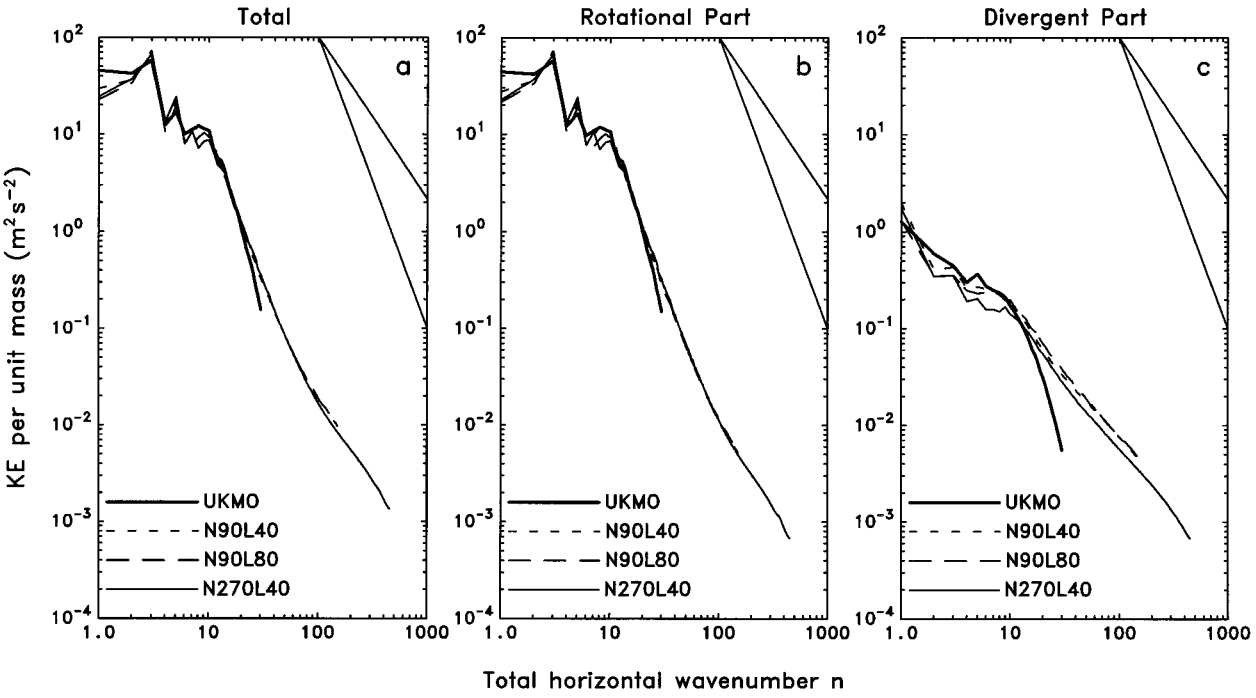

FIG. 4. Jul mean KE spectra as a function of total horizontal wavenumber for three versions of the SKYHI model with different resolution. Spectra calculated from UKMO assimilated data averaged over the 5 Julys from 1993 to 1997 are shown for comparison. The UKMO spectra are truncated at $N = 30$, the N90 spectra at $N = 150$, the N270 spectra at $N = 450$, and all curves represent vertical means over the 92–353-mb layer. Shown are (a) the total KE spectrum, (b) the rotational part of the total KE spectrum, (c) the divergent part of the total KE spectrum. Straight lines in the upper right-hand corner of each panel have slopes of -3 and $-5/3$.

modes with $m \approx n$ only. These modes correspond to spherical harmonic basis functions with maximum values confined to equatorial regions. The anisotropy of the spectrum in equatorial regions ($m \approx n$) is consistent with the results of Fig. 2d, where different results are obtained depending on whether the sampling is done along north–south or east–west sections. At planetary and subplanetary scales $\mathcal{E}_{n,m}$ depends strongly on both n and m, in agreement with the large-scale anisotropy seen in Figs. 2a–c. Figure 3 also agrees well with $E_{n,m}$ calculated from observational data by Boer (1994) and Boer and Shepherd (1983).

In the following sections, quantities will be shown as functions of the total wavenumber n alone, by summing over the zonal wavenumber m, that is,

$$\mathcal{E}_n(p, t) = \frac{1}{4}\frac{a^2}{[n(n+1)]}\sum_{m=-n}^{n}(|\zeta_{n,m}(p, t)|^2 + |\delta_{n,m}(p, t)|^2), \tag{6}$$

and similarly for $E_n(p, t)$ obtained from (3).

b. Results

July mean upper-tropospheric KE spectra per unit mass, $\mathcal{E}_n$, are shown in Fig. 4 for the three SKYHI versions. The spectrum calculated from U.K. Met. Office (UKMO) analyzed winds (Swinbank and O'Neill 1994) is shown for comparison. The UKMO data, originally analyzed on a 96×72 latitude–longitude grid, are truncated at $N = 30$ (T30).

There is good qualitative agreement between the three model versions and the UKMO result in the total KE at planetary and synoptic scales, although the models underestimate the observed value at $n = 1$ by a factor of ~ 2. For wavenumbers $10 \lesssim n \lesssim 20$, all spectra show power-law behavior with a slope ~ -3, in agreement with the theories of 2D and quasigeostrophic turbulence and with previous observational and modeling studies (Charney 1971; Boer and Shepherd 1983; Laursen and Eliasen 1989; Koshyk and Boer 1995; Koshyk et al. 1999a,b). For $n \gtrsim 20$, the UKMO spectrum drops off significantly faster than the simulated spectra. This feature of assimilated datasets has been discussed elsewhere (Koshyk and Boer 1995; Koshyk et al. 1999a) and is reasonably attributed to the lack of adequate global data coverage at these wavenumbers. For $n \gtrsim 80$, model spectra become shallower, with a clear transition from the large-scale ~ -3 slope to the mesoscale $\sim -5/3$ slope.

Comparison of Figs. 4b and 4c indicates that the rotational component of the flow dominates the divergent component for all scales $n \lesssim 100$. The agreement between the N90 and N270L40 rotational KE spectra (Fig. 4b) is good, especially in the two power-law ranges.

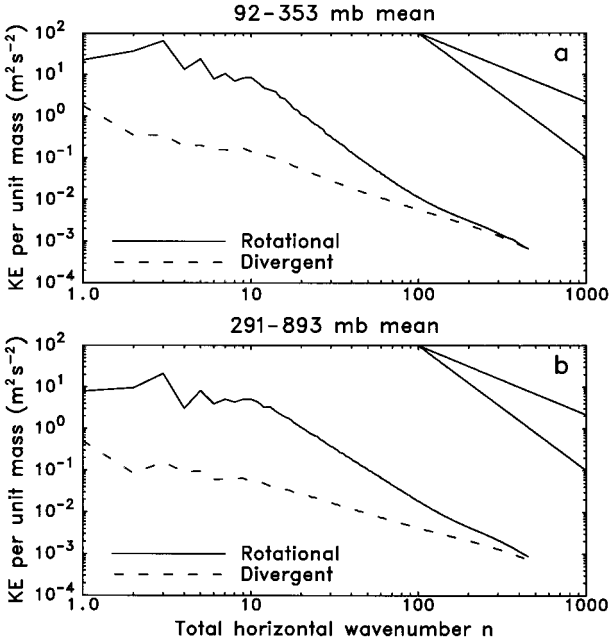

FIG. 5. N270L40 Jul mean rotational and divergent KE spectra vs total horizontal wavenumber vertically averaged over the (a) 92–353-mb layer, (b) the 291–893-mb layer.

The agreement between the divergent spectra is poorer (Fig. 4c) as the N90L40 and N90L80 spectra differ from each other for a broad range of medium-valued wavenumbers and both of the N90 spectra differ significantly from the N270L40 spectrum at all wavenumbers. This reveals some inadequacy in the subgrid-scale parameterization schemes in SKYHI and the way that they scale with model resolution.

Yuan and Hamilton (1994) derived a similar conclusion from idealized shallow-water model simulations at different spatial resolutions. The small-scale dissipation in their experiments was provided by a hyperviscosity that was scaled with the grid spacing. They found that for the balanced component of the flow, the high-resolution model spectrum very closely corresponds to a lower-resolution model spectrum over the common range of resolved wavenumbers. By contrast, the residual or unbalanced part of the spectrum shows sensitivity to the model resolution, suggesting a deficiency in the standard diffusive treatment of subgrid-scale effects for models that support divergent motions (see Fig. 10 of Yuan and Hamilton).

As noted in the introduction, the mechanism underlying the observed $-5/3$ spectral regime is the subject of some controversy. It is understood either as a low–Froude number quasi-2D inertial subrange dominated by the rotational part of the flow (Lilly 1983; Gage and Nastrom 1986; Vallis et al. 1997) or a regime characterized by a spontaneously generated gravity wave (divergent) component in the flow (Polvani et al 1994; Yuan and Hamilton 1994; Bartello 1995). Figure 5a shows the rotational and divergent parts of the upper-tropospheric KE spectrum for the N270L40 run. The spectrum for wavenumbers $n \lesssim 100$ is dominated by the rotational part of the flow. At mesoscales ($n \gtrsim 100$) the rotational and divergent parts of the flow are similar in amplitude. Figure 5b shows the same quantities averaged over a deeper tropospheric layer. Here the rotational part of the flow dominates the divergent part for all but the smallest ~ 50 wavenumbers.

In order to actually separate the flow into balanced and unbalanced (free gravity wave) components, a high-order balance approximation is required. Such an approach is beyond the scope of this study. However, the presence of strong divergent components in the mesoscale of the SKYHI model is consistent with the presence of resolved gravity waves, indicating that the $-5/3$ spectral regime is not a quasi-2D inertial subrange. There is ample evidence from space–time analyses of SKYHI results for the presence of vertically propagating gravity waves in the models (e.g., Hamilton and Mahlman 1988; Hayashi et al. 1989; Manzini and Hamilton 1993).

5. Spectral kinetic energy budget for the troposphere

a. Formalism

The physical processes contributing to the simulated spectra in Figs. 3–5 can be quantified by computing the spectral KE budgets for the different model versions. This requires knowledge of the contribution from each term in the prognostic model equation for KE at each wavenumber *n*. The horizontal momentum equations for the models used here in regions where model levels coincide with pressure levels ($p < 353$ mb) are given by

$$\frac{\partial u}{\partial t} = -\nabla \cdot (u\mathbf{u}) + fv - \frac{1}{a\cos\phi}\frac{\partial \Phi}{\partial \lambda} + F_\lambda^H + F_\lambda^V \quad (7a)$$

$$\frac{\partial v}{\partial t} = -\nabla \cdot (v\mathbf{u}) - fu - \frac{1}{a}\frac{\partial \Phi}{\partial \phi} + F_\phi^H + F_\phi^V, \quad (7b)$$

where $\mathbf{u} = (u, v, \omega)$ is the three-dimensional velocity field; ∇ is the three-dimensional divergence operator; $f = 2\Omega \sin\phi$ is the Coriolis parameter; Φ is geopotential height; and F^H and F^V are the parameterized subgrid-scale forcing terms in the horizontal and vertical directions, respectively, described in section 2. (Note that familiar metric terms appear when the divergence term is fully expanded.) The five terms on the right-hand sides of (7a) and (7b) will be referred to, in order, as total advection, Coriolis, pressure gradient, horizontal diffusion, and vertical diffusion terms. Horizontal and vertical parts of the total advection term are not uniquely defined and depend on whether the model equations are written in flux form or in advective form.

The spectral KE budget is obtained by calculating

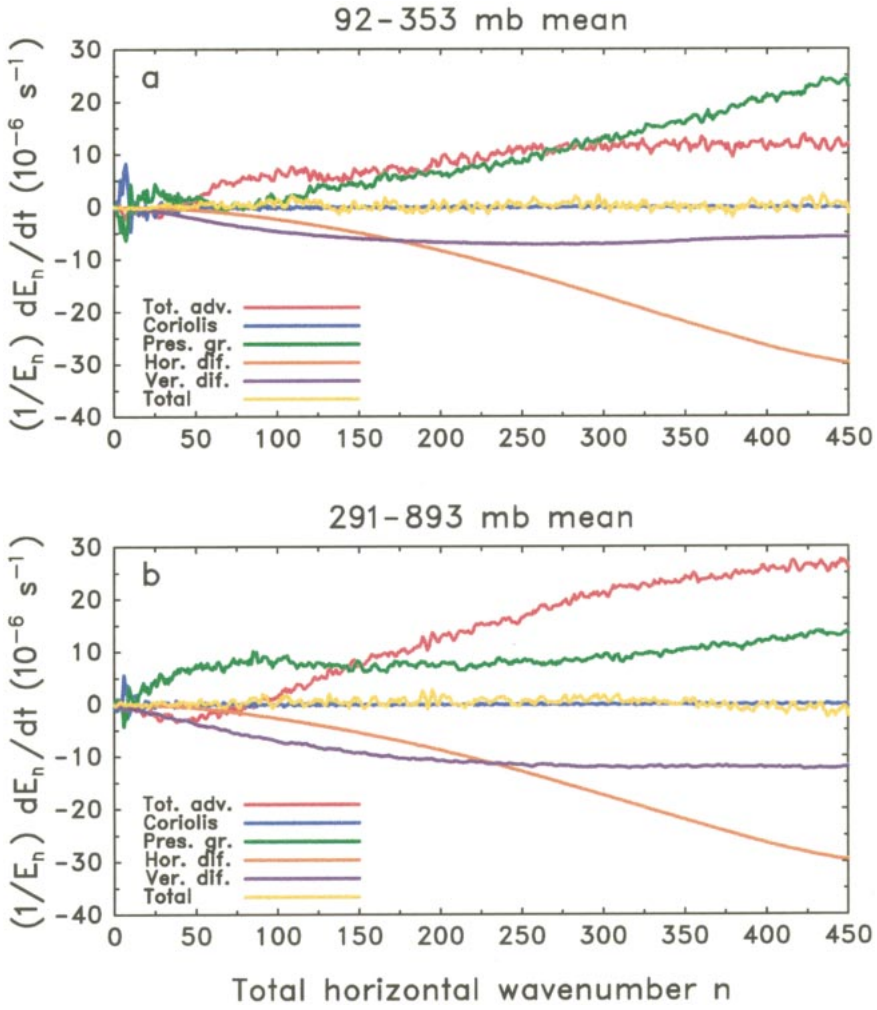

FIG. 6. N270L40 Jul mean KE budgets vs total horizontal wavenumber for the (a) 92–353-mb layer, (b) 291–893-mb layer. The terms contributing to the KE budget together with their total are shown in each panel. The curves are scaled at each wavenumber by the vertically integrated KE spectrum in each layer.

each term on the right-hand side of (7) on the SKYHI grid, using finite differences to approximate derivatives (Smagorinsky et al. 1965, appendix I). The resulting fields are interpolated to a Gaussian grid and spectrally transformed to obtain spherical harmonic coefficients for each field. Differentiating (3) with respect to time gives

$$\frac{\partial E_n^m}{\partial t} = \frac{1}{4}\left[u^*_{n,m}\left(\frac{\partial u}{\partial t}\right)_{n,m} + u_{n,m}\left(\frac{\partial u}{\partial t}\right)^*_{n,m} + v^*_{n,m}\left(\frac{\partial v}{\partial t}\right)_{n,m} + v_{n,m}\left(\frac{\partial v}{\partial t}\right)^*_{n,m}\right], \quad (8)$$

where the * denotes a complex conjugate. Pairwise substitution of zonal and meridional advection, Coriolis, pressure gradient, horizontal diffusion, and vertical diffusion terms for $(\partial u/\partial t)_{n,m}$ and $(\partial v/\partial t)_{n,m}$ in (8) yields a total of five terms in the spectral KE budget. These terms are expected to approximately cancel one another on the monthly mean, since the terms on the left-hand sides of (7a) and (7b) are small for this averaging period.

For $p > 353$ mb the wind fields are interpolated or extrapolated from model levels to standard pressure levels, and the geopotentials are calculated on the standard pressure levels. The terms in the momentum budget are then reconstructed approximately using the fields on pressure levels. This leads to some imbalance in the total KE budget compared to levels for which $p < 353$ mb, but the effects are very small and are confined to small spatial scales.

b. *N270 results*

Figure 6 shows the spectral KE budgets as a function of n for the N270L40 model vertically averaged over

the 92–353-mb layer and 291–893-mb layer. All terms in the budget are scaled by E_n for each n to yield characteristic timescales for each physical process. This scaling highlights the features of the budget at intermediate and large wavenumbers, since the budget terms actually take their largest values at wavenumbers ~1–10.

The effect of the total nonlinear advective terms (horizontal plus vertical) in Fig. 6 is to remove KE from small wavenumbers and add KE to larger wavenumbers in both the 92–353-mb layer and, to a greater extent, in the 291–893-mb layer. The advective contribution to the KE at mesoscales is quite substantial—at most wavenumbers it is comparable to, or even larger than, the other positive contribution from the pressure gradient term. The removal of KE from large scales and the addition of KE to small scales is consistent with a downscale KE cascade, although, because of the presence of a divergent component in the flow, neither the total nor the horizontal advection terms acts solely to redistribute KE among scales. Integrated over a pressure slab, the advection term for a particular wavenumber can be regarded as a sum of nonlinear cascades from all other wavenumbers and an advective flux of KE at that wavenumber through the upper and lower boundaries of the slab. The positive contribution to the KE in the mesoscale appears to occur for all the pressure intervals examined here from at least 1 to 891 mb (see Fig. 13b). This suggests that the internal nonlinear horizontal cascade is responsible for helping to energize the mesoscale over most of the model atmosphere. The downscale KE cascade has also been seen in previous studies using assimilated and model-generated data, at wavenumbers $n \gtrsim 30$ (e.g., Boer and Shepherd 1983; Koshyk and Boer 1995).

The Coriolis term in Fig. 6 makes a nonzero contribution to the KE budgets, and its effects are most pronounced at large scales, where it is in approximate geostrophic balance with the pressure gradient term. The Coriolis force, of course, does no net work, and its contribution to the global mean KE budget (obtained by summing the contributions from each n) is 0. In the f-plane case, the Coriolis contribution to KE at *each* Fourier wavenumber is identically zero. The situation is more complicated in the spherical case because the product of the Coriolis parameter (proportional to sine of latitude) and a spherical harmonic of order n is proportional to a sum of spherical harmonics of orders $n - 1$ and $n + 1$. Thus the Coriolis force acts to ''spread'' KE to adjacent wavenumbers without changing the total amount.

A prominent KE source in Figs. 6a,b is the pressure gradient term. It is well known that when the pressure gradient term in the physical space KE budget is integrated over some volume, it can be expressed as the sum of a boundary work term and a volume integral representing the internal conversion of potential energy to kinetic energy. For plane geometry with periodic boundary conditions, this decomposition can actually be done separately for each individual Fourier component, that is, using the continuity and hydrostatic relations

$$\left(\frac{\partial E}{\partial t}\right)_{k,l}^{\mathrm{PG}} = -u_{k,l}\left(\frac{\partial \Phi}{\partial x}\right)_{k,l}^{*} - \upsilon_{k,l}\left(\frac{\partial \Phi}{\partial y}\right)_{k,l}^{*} - u_{k,l}^{*}\left(\frac{\partial \Phi}{\partial x}\right)_{k,l} - \upsilon_{k,l}^{*}\left(\frac{\partial \Phi}{\partial y}\right)_{k,l}$$
$$= -\frac{\partial}{\partial p}(\Phi_{k,l}\omega_{k,l}^{*} + \Phi_{k,l}^{*}\omega_{k,l}) - \frac{R}{p}(T_{k,l}\omega_{k,l}^{*} + T_{k,l}^{*}\omega_{k,l}), \tag{9}$$

where subscripts on a variable denote its Fourier coefficients, k and l are wavenumbers in the x and y directions, and the superscript PG refers to the KE tendency associated with the pressure gradient term. Upon vertical integration of (9) from pressure level p_{bottom} to p_{top}, a sum of three terms is obtained: gravitational potential energy flux into the layer at p_{bottom}, gravitational potential energy flux out of the layer at p_{top}, and conversion from KE to total potential energy within the layer. A similar decomposition was discussed by Lambert (1984) but beginning with the expression (5) for $\mathcal{E}_{n,m}$ rather than (9).

There is no exact analog to (9) when spherical harmonic basis functions are used. However, (9) is approximately satisfied in practice when the indices k and l are replaced by n and m. Figure 7a shows the pressure gradient term reproduced from Fig. 6a (the ''actual'' pressure gradient term), together with the ''approximate'' pressure gradient term obtained from (9) after replacing (k, l) with (n, m) and scaling by E_n. There is good agreement between the two curves. Figure 7b shows the individual terms composing the approximate pressure gradient term in the upper troposphere: conversion of KE to total potential energy in the 92–353-mb layer, the gravitational potential energy flux at 92 mb, and the gravitational potential energy flux at 353 mb, all scaled by E_n at each wavenumber. (Note that the flux terms are divided by the pressure difference across the layer, to remain consistent with the vertical averaging of the conversion term.) The conversion term is positive for $n \lesssim 150$, indicating a conversion from total potential energy to KE, and it is the dominant contribution for most $n \lesssim 50$. At larger n the conversion contribution is overwhelmed by the boundary pressure work terms. For $n \gtrsim 100$ the upward flux into the bottom of the layer exceeds the flux through the top of the layer. Thus, over most of the mesoscale, the pressure gradient term in Fig. 6a largely represents a convergence of mechanical fluxes such as would be expected from vertically propagating gravity waves, forced from below and partially dissipated in the upper-tropospheric layer considered.

Figure 7c shows that the picture in the 291–893-mb

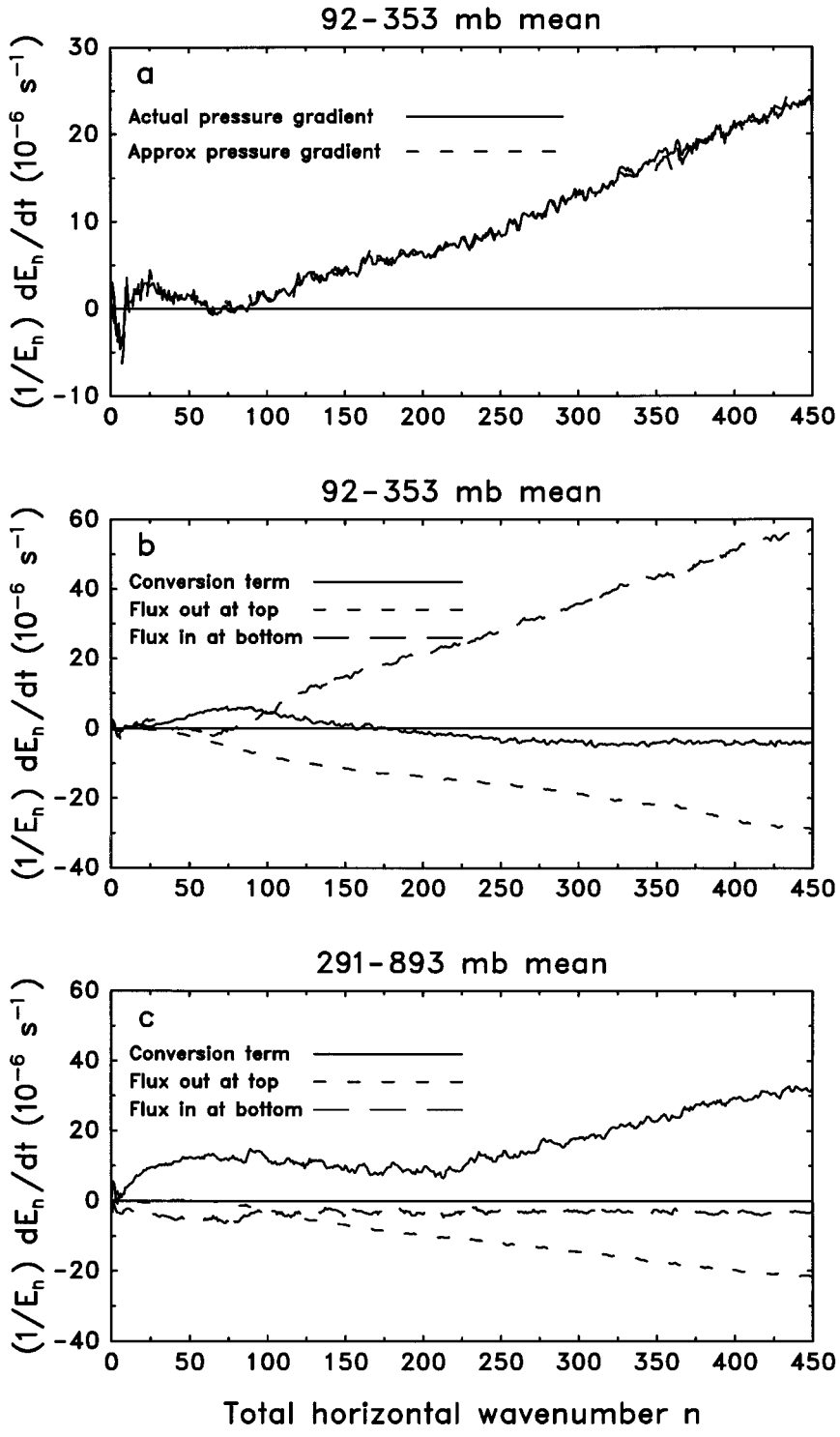

FIG. 7. Approximate contributions to the pressure gradient term shown in Fig. 6: (a) the actual pressure gradient term (reproduced from Fig. 6a) and an approximation to this term for the 92–353-mb layer; (b) the three terms composing the approximate pressure gradient term in (a); (c) as (b) but for the 291–893-mb layer.

layer is completely different. The largest term at all wavenumbers is the conversion term from total potential energy to KE, which is opposite in sign to the conversion term in the upper troposphere for $n \gtrsim 150$. The flux into the bottom of the layer is extremely weak and actually negative for a wide range of wavenumbers, in contrast to the dynamics of the upper troposphere. The somewhat stronger gravitational potential energy flux at 291 mb is indicative of gravity wave generation in the 291–893-mb layer.

The mainly positive contributions from the advective and pressure gradient terms in Fig. 6 are balanced by the effects of subgrid-scale momentum diffusion. The dissipation rate (inverse timescale) for the horizontal diffusion scales roughly as the square of the wavenumber, as expected [see (1)]. The vertical diffusion dissipation rates also rise with the horizontal wavenumber for a range of n, which presumably reflects a correlation between small horizontal-scale and small vertical-scale features. However, the dependence of the vertical diffusive dissipation rate on n is approximately linear to $n \sim 75$ and is approximately constant for all $n \gtrsim 100$. The timescale for the vertical diffusion in the $n \gtrsim 100$ range is about 2 days in the upper troposphere and less than 1 day in the lower-troposphere region. By contrast, the horizontal diffusion rates are very similar in the two layers. The stronger vertical diffusive dissipation rates in the lower troposphere are likely associated with planetary boundary layer processes.

The present analysis produces a fairly clear picture of the energetics that maintain the model KE in the mesoscale. In the upper-tropospheric layer considered here, encompassing the heights of the GASP data analyzed by Nastrom et al. (1984), the KE at mesoscale wavenumbers is supplied by two processes: a downscale nonlinear cascade from larger scales and the propagation of energy from below (presumably as gravity waves). The KE is lost in this layer by upward propagation of waves through the top boundary and by both vertical and horizontal parameterized subgrid-scale momentum diffusion. The mesoscale KE in the lower troposphere is forced by a downscale nonlinear cascade from larger scales and by conversion from total potential energy. Dissipation is provided by horizontal and vertical diffusion, as in the upper troposphere, although vertical diffusion is somewhat stronger in the lower layer. Some mesoscale KE also escapes the lower troposphere in the form of upward-propagating internal gravity waves.

c. N90 results

The KE budgets corresponding to Fig. 6 for the N90L40 and N90L80 runs are shown in Figs. 8a and 8b. The N270L40 budget (Fig. 6c) for wavenumbers $0 \leq n \leq 150$ only is shown in Fig. 8c for direct comparison. The Coriolis term and total budget term have been omitted since the former makes little contribution to the budget for $n \gtrsim 10$ and the latter is very close to zero for all wavenumbers. The overall picture for the maintenance of the KE in the mesoscale is similar in both N90 versions and in the N270 version. In all three model versions there are positive contributions to the KE budget for $n \gtrsim 75$ from both the pressure gradient and nonlinear triad terms. The horizontal diffusion term is much stronger in the N90 versions for $n \lesssim 150$, and positive contributions from pressure gradient terms are also stronger.

One interesting aspect of the N90 versus N270 comparison concerns the role of vertical and horizontal subgrid-scale diffusion. At any given wavenumber the timescale for the horizontal diffusion term in the N90 versions is almost an order of magnitude shorter than that at N270, consistent with expectations [see Eq. (1)]. By contrast, the vertical diffusive timescales are actually quite similar in the N90L40 model and the version with doubled vertical resolution (N90L80). At N90 the horizontal diffusion is larger than the vertical diffusion for the KE budget at almost all wavenumbers (Fig. 8). The situation at N270 is different—the vertical diffusion dominates for over half the resolved wavenumber range (Fig. 6). It seems reasonable to expect this pattern to continue if model horizontal and vertical resolutions were to be increased even further, so that the spectral slopes will become insensitive to details of the horizontal diffusion parameterization for a broad range of wavenumbers.

6. N270 regional KE spectra

A shortcoming of the global spherical harmonic framework is that information about the dynamics in certain regions of the atmosphere (e.g., the Tropics alone) is difficult to obtain. However, some progress in this direction can be made by masking a global grid with a function that equals 1 in the region of interest and equals 0 outside the region of interest. The spectrum obtained by transforming the resulting field should contain information from the region of interest only, although it will be contaminated somewhat by the nature of the transition between the region of interest and the surrounding area.

In order to investigate the contribution to the total N270L40 KE spectrum shown in Fig. 4 from three separate regions (the Northern Hemisphere extratropics, the Tropics, and the Southern Hemisphere extratropics), global masks are constructed using hyperbolic tangent functions with maximum and minimum values of 1 and 0, respectively. The Northern Hemisphere extratropics is defined as the region north of 20°N, the Southern Hemisphere extratropics as the region south of 20°S, and the Tropics as the region between 20°N and 20°S. Adding the spectra obtained from masked grid fields for these three regions yields the dashed curve in Fig. 9, which is shown together with the actual total N270L40 KE spectrum, $\mathcal{E}_n$, from Fig. 4a (solid curve). The good comparison between the solid and dashed curves in Fig.

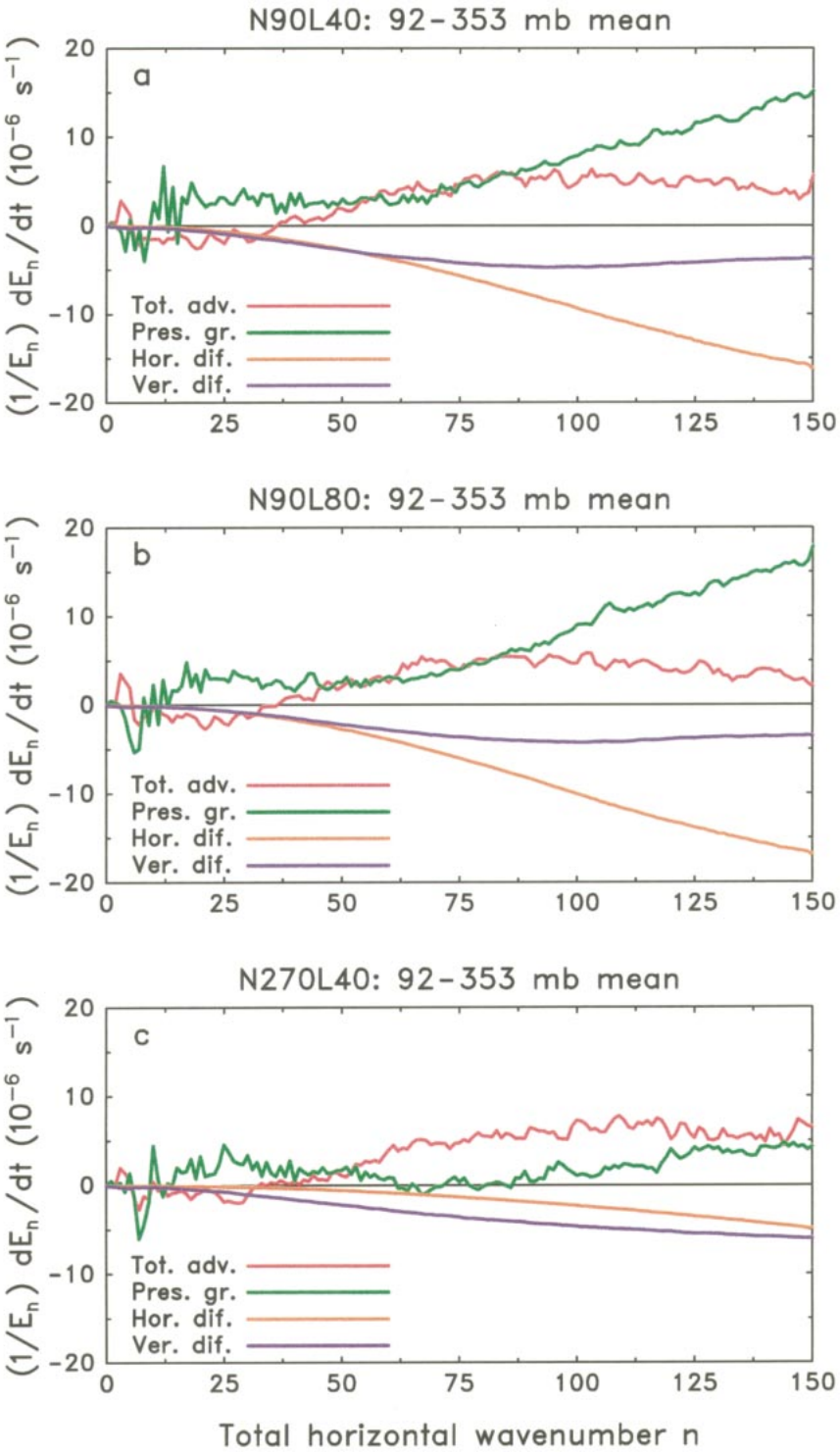

FIG. 8. Terms in the Jul mean KE budget vs total horizontal wavenumber for the 92–353-mb layer: (a) N90L40 model version, (b) N90L80 model version, (c) N270L40 version (as Fig. 6a but for the wavenumber range $n = 0$–150 only).

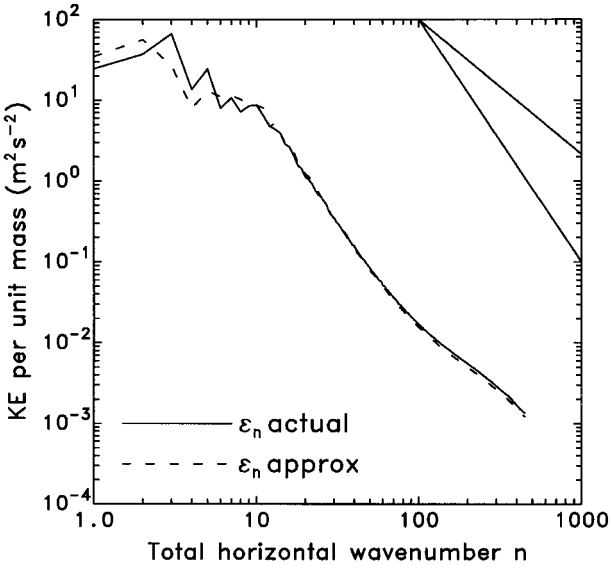

FIG. 9. N270L40 Jul mean KE spectrum vs total horizontal wavenumber reproduced from Fig. 4a (solid), and an approximation to the spectrum obtained by summing spectra calculated for three different latitude bands (dashed).

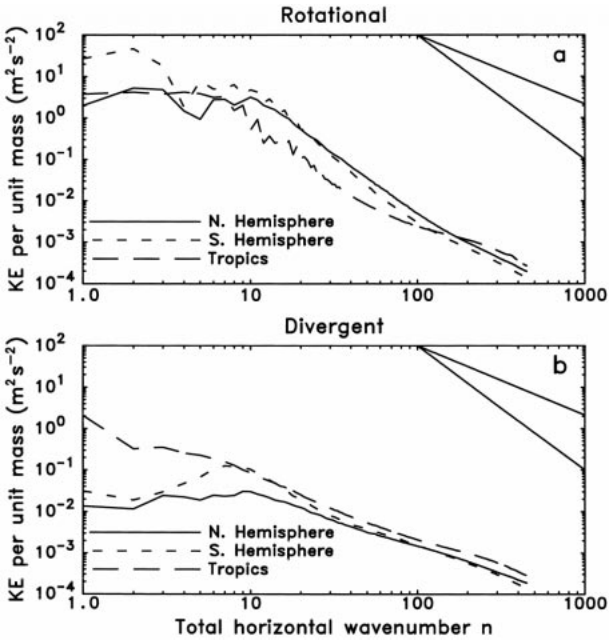

FIG. 10. N270L40 Jul mean KE spectra vs total horizontal wavenumber averaged over the 92–353-mb layer for the Northern Hemisphere (20°–90°N), the Tropics (20°S–20°N), and the Southern Hemisphere (90°–20°S): (a) rotational parts, (b) divergent parts.

9 for $n \gtrsim 10$ provides some confidence in assessing the contributions to the total spectrum from each of the regions of interest, at least for $n \gtrsim 10$. Changing the width of the transition region used for the masks from 5° to 20° has virtually no effect on the approximate spectrum for $n \gtrsim 10$, although there is strong sensitivity to this change at smaller wavenumbers.

Figure 10 shows the contribution from each region to the rotational and divergent parts of the global KE spectrum, $\mathcal{E}_n$, shown in Fig. 9. Planetary scales (small wavenumbers) are dominated by the rotational component throughout, with the main contribution from the Southern (winter) Hemisphere. The major contribution to the divergent part of the flow at planetary scales comes from the Tropics. Differences between the rotational and divergent parts are minimized in the Tropics where they are negligible for $n \gtrsim 100$. This is consistent with the observational study of Cho et al. (1999a), who found that the divergent energy actually exceeds the rotational energy in tropical regions. Values of KE at mesoscales are generally largest in the Tropics for both rotational and divergent components, with the smallest contributions coming from the Southern Hemisphere.

7. Spherical harmonic spectra and spectral budgets for the middle atmosphere

July mean KE spectra vertically integrated over the 0.91–149-mb layer are shown in Fig. 11. Agreement between the three models and the UKMO assimilated data is qualitatively good for the total KE at wavenumbers $n \lesssim 20$. The total simulated KE spectra show two power-law regimes, as in the troposphere, but they are different in character. There exists a large-scale regime with a slope steeper than -3 and a relatively smaller-scale regime with a slope close to -1. The transition between these regimes occurs at $n \sim 20$ or a wavelength of approximately 2000 km. This is well upscale of the $n \sim 80$ (~500 km) transition wavenumber seen in the upper-tropospheric N270L40 spectrum (Fig. 4). The spectral slope in the large-scale regime is steeper than in the troposphere because Charney–Drazin filtering (Charney and Drazin 1961) has eliminated much of the subplanetary- and synoptic-scale eddy activity, yielding lower spectral amplitudes at these scales (Koshyk et al. 1999a). At smaller scales, the stratospheric spectrum is shallower and the divergent component actually exceeds the rotational component for $n \gtrsim 30$ in all of the model versions. This presumably indicates the presence of tropospherically forced gravity waves, which, of course, are not subject to the Charney–Drazin filtering at subplanetary scales.

The largest discrepancy between the N90 and N270 model versions is in the divergent component of the KE (Fig. 11c). An implication of this is that subgrid-scale processes associated with the divergent part of the flow are not properly represented by the subgrid-scale parameterization schemes used in SKYHI. The divergent part of the UKMO assimilation decreases rapidly for $n \gtrsim 10$, indicating an extreme amount of divergence damping in the assimilation model.

July mean KE spectra vertically integrated over the 0–1.28-mb layer are shown in Fig. 12. The upper boundary of the UKMO assimilated dataset is at 0.3 mb so

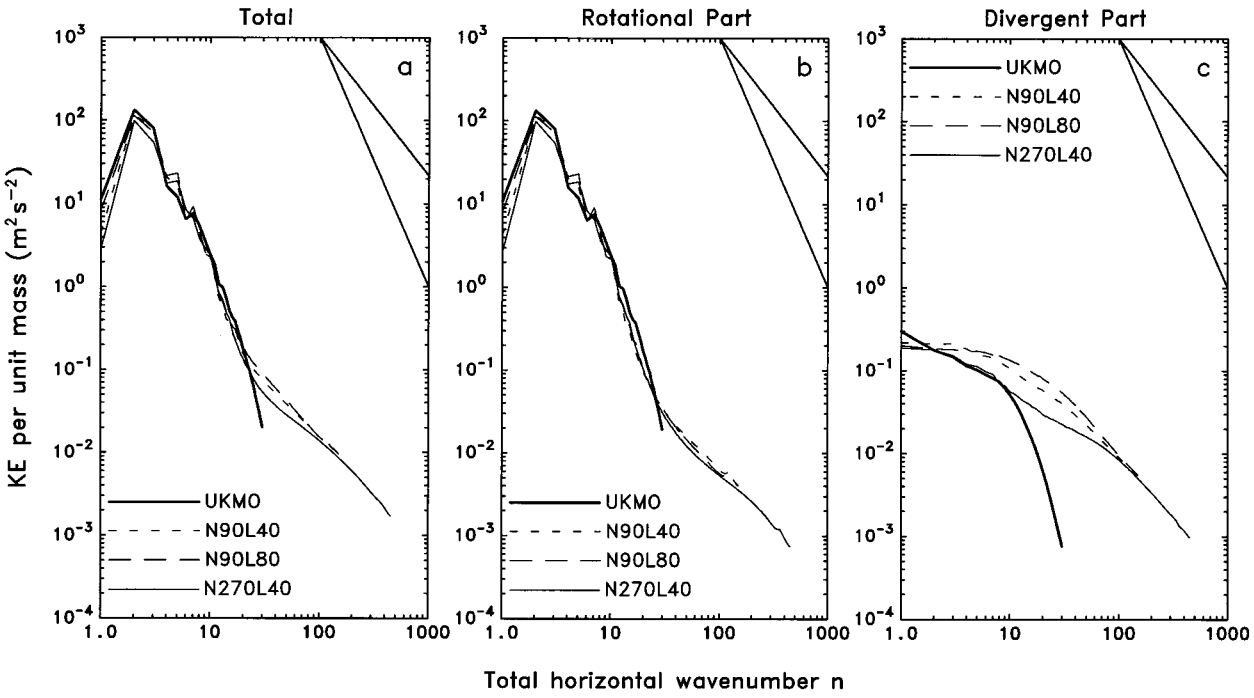

FIG. 11. As Fig. 4 but for the 0.91–149-mb layer.

no observational data comparison is shown. As in the stratosphere, two distinct power-law regimes are evident in the total spectra. The transition from a steep to a shallow spectral slope occurs at a lower wavenumber in the mesosphere ($n \sim 10$) than in the stratosphere ($n \sim 20$) for all model versions. The same result is also seen in other middle-atmosphere GCMs (Koshyk et al. 1999a).

There are differences in the spectral amplitudes of total KE among all three model versions for $n \gtrsim 20$.

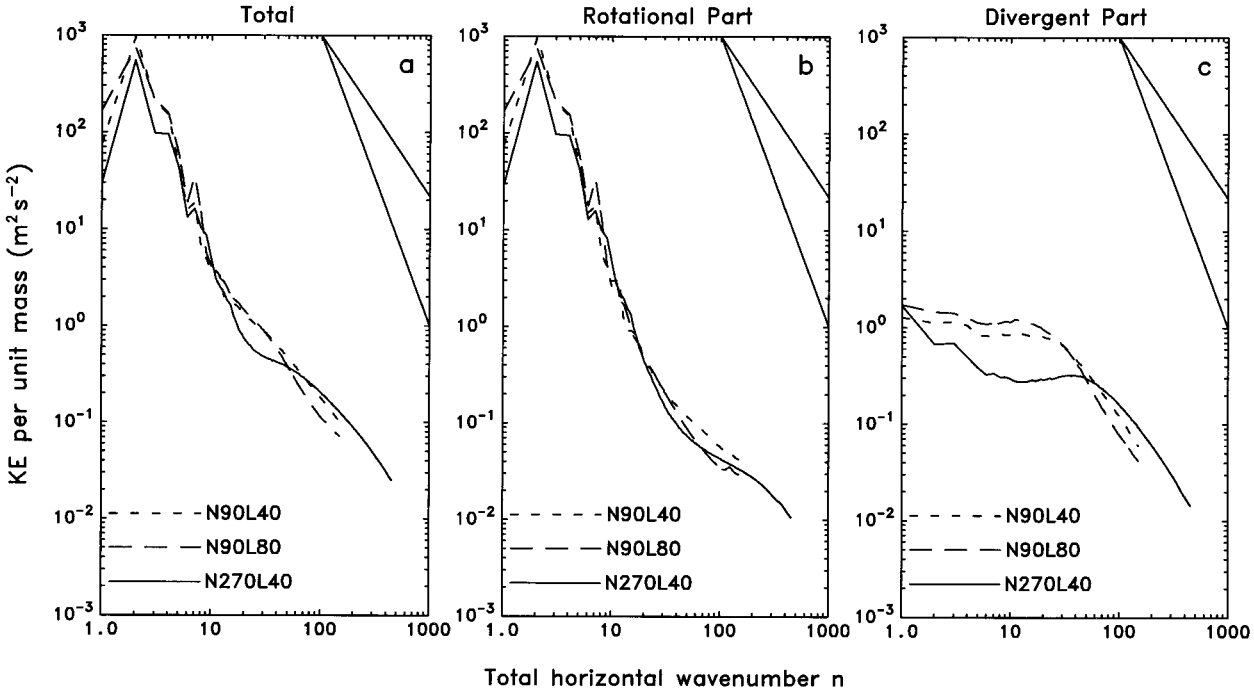

FIG. 12. As Fig. 4 but for the 0–1.28-mb layer. A suitable observed KE spectrum for this layer is not available for comparison.

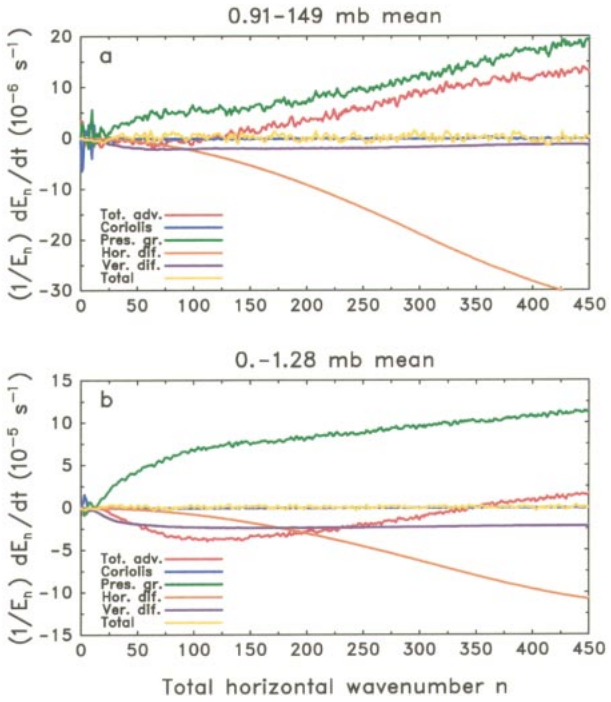

FIG. 13. As Fig. 6 but for the (a) 0.91–149-mb layer, (b) 0–1.28-mb layer.

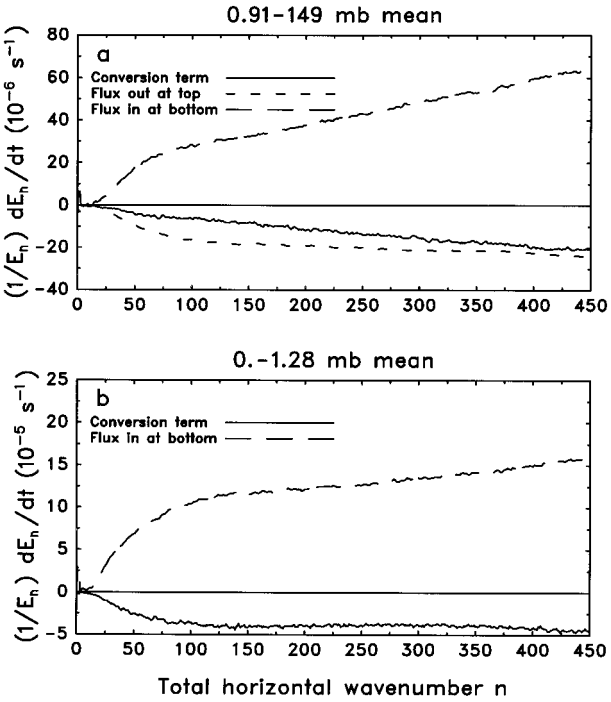

FIG. 14. As Fig. 7b but for the (a) 0.91–149-mb layer, (b) 0–1.28-mb layer. The ''flux out at top'' curve is omitted from (b) since it vanishes at 0 mb.

This is mainly the result of differences in the divergent component (Fig. 12c). At $n \sim 10$, the N90 and N270L40 divergent spectra differ by a factor of almost 10. The divergent spectra are comparable in magnitude to the rotational spectra for most wavenumbers, excluding the largest decade where the rotational component dominates. The poor agreement among the spectra of Fig. 12 at different resolutions should be considered together with the significant differences in the simulated zonal-mean middle-atmospheric climatology at different resolutions (Hamilton et al. 1999). The Southern Hemisphere polar night jet is reduced significantly in strength in the N270 model relative to that in the N90 versions. The N90L80 version has much stronger shears in the tropical stratosphere and mesosphere than either of the L40 versions. These changes in the mean flow will result in different filtering of vertically propagating waves among the models, potentially having important consequences for the KE spectra in the mesosphere.

Figure 13 shows the stratospheric (0.91–149 mb) and mesospheric (0–1.28 mb) KE budgets for the N270L40 model. Figure 13a can be compared to Fig. 6, where corresponding tropospheric budgets are shown. The total diffusion and pressure gradient terms are similar for the upper-troposphere and stratosphere regions, but the vertical diffusion is less significant in the stratosphere. Unlike the troposphere, where total advection dominates the pressure gradient term for a finite range of wavenumbers, the pressure gradient term provides the dominant positive contribution to the KE budget at all wavenumbers in the stratosphere. Figure 13b shows that the dynamical picture in the mesosphere is similar, except that the pressure gradient term now clearly dominates the positive contribution at all wavenumbers and the total advection term is negative at all but the largest wavenumbers. The vertical diffusion dominates the horizontal diffusion over the first ~1/3 of the resolved spectral range (vs only the first ~1/6 in the stratosphere). This presumably reflects the dissipation associated with breaking gravity waves that trigger the vertical diffusion parameterization at small local Richardson number.

Figure 14 shows the components of the pressure gradient term in the (Fig. 14a) stratosphere and (Fig. 14b) mesosphere. The stratosphere is driven mainly by a flux from below, part of which exits the layer into the mesosphere above and the remainder of which is dissipated within the stratosphere or converted to gravitational potential energy. This is qualitatively similar to the energetics of the upper troposphere (Figs. 6a and 7b). In the mesosphere, there is no vertical flux through the top boundary since the top coincides with the model upper boundary, where the vertical velocity vanishes. Figure 14b confirms the commonly held view that gravity wave fluxes play a dominant role in the mesospheric circulation as the pressure gradient term is dominated by the flux through the 1.28-mb level. The flux into the mesosphere is also much larger than that into the stratosphere (note different scaling in Figs. 14a and 14b).

As noted earlier, the zonal-mean flow in the SKYHI middle atmosphere is a strong function of model res-

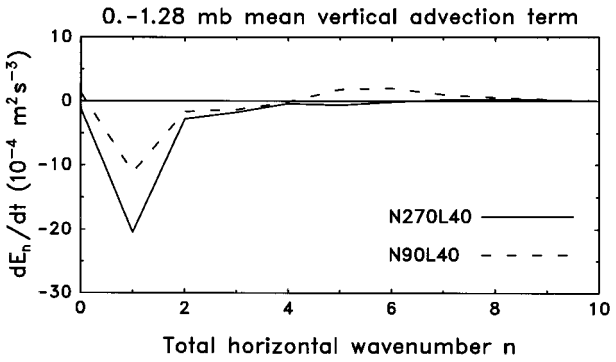

FIG. 15. The contribution to the KE budget from vertical advection for the N270L40 and N90L40 versions of SKYHI, vertically averaged over the 0–1.28-mb layer. The curves are not scaled by the KE spectrum, and only the large-scale wavenumber part of the spectrum (n = 0–10) is shown.

olution, and this is especially true in the vicinity of the Southern Hemisphere polar night jet. In all versions, the model generates a zonal drag on the jet through a divergence of the vertical eddy momentum flux associated with gravity waves. As the model horizontal resolution is increased, the resolved eddy fluxes and the resulting drag on the zonal-mean flow become stronger (Hamilton et al. 1995; Jones et al. 1997). The vertical advection terms for the N90L40 and N270L40 models, averaged over the 0–1.28-mb layer, are shown in Fig. 15. The vertical advection is defined here using the standard flux form of the advection term. Although the partitioning of the total advection term into horizontal and vertical parts is somewhat arbitrary, Fig. 15 provides at least a qualitative measure of the behavior of triad terms associated with vertical advection. The result at $n = 1$ in Fig. 15 shows that KE is dissipated by the vertical advection term, and this dissipation becomes stronger as horizontal resolution is increased.

8. Discussion and conclusions

Some of the basic results of this study are summarized in Fig. 16, where total, rotational, and divergent parts of the GFDL SKYHI N270L40 KE spectrum as a function of total horizontal wavenumber for the upper troposphere (92–353 mb), stratosphere (0.91–149 mb), and mesosphere (0–1.28 mb) are shown. The total KE spectrum in the troposphere shows two power-law ranges: a large-scale regime ($10 \lesssim n \lesssim 80$) with a slope ~ -3 and a mesoscale regime ($n \gtrsim 80$) with a slope $\sim -5/3$. This is in agreement with the observational study of Nastrom et al. (1984) and was discussed in Koshyk et al. (1999b). The rotational part of the flow dominates the large-scale regime, and there is approximate equipartition between rotational and divergent parts of the flow in the mesoscale regime. These results suggest that the mesoscale regime is not well approximated by 2D, low–Froude number balance but contains a significant gravity wave or unbalanced component.

Generally, at any given altitude, the KE spectrum is dominated by the rotational part of the flow for a range

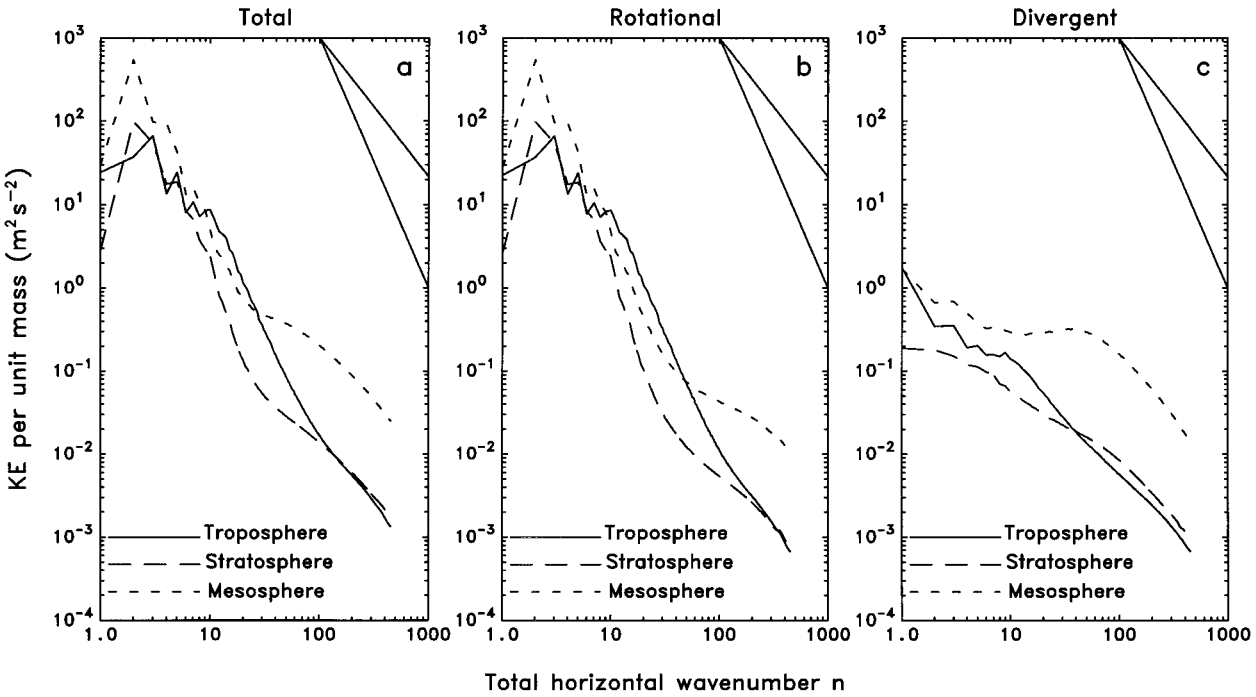

FIG. 16. N270L40 Jul mean KE spectra vertically averaged over the upper troposphere (92–353 mb), stratosphere (0.91–149 mb), and mesosphere (0–1.28 mb): (a) total KE spectrum, (b) rotational part of the KE spectrum, (c) divergent part of the KE spectrum.

of scales $n \lesssim n_*$. For scales $n \gtrsim n_*$, the power in the divergent component is comparable to, or exceeds, that in the rotational component. The wavenumber n_* decreases with altitude, taking a value of $\sim$100 in the upper troposphere and decreasing to a value of $\sim$10 in the upper mesosphere. The reason for the variation of n_* with height is the comparatively more rapid increase of the divergent component compared to the rotational component (Koshyk et al. 1999a). The wavenumber n_* defined this way is also close to the wavenumber marking the break seen in the total KE spectra between a large-scale power-law regime with steep slope and a relatively more shallow power-law regime.

Comparison of spectra between two different horizontal resolution versions of the SKYHI model suggests that the horizontal subgrid-scale parameterization in the lower-resolution model does not properly represent the effects of unresolved horizontal scales at most altitudes. For the divergent part of the flow, agreement between high- and low-resolution models is poor at all altitudes considered; for the rotational part of the flow, agreement is good in the troposphere, fair in the stratosphere, and poor in the mesosphere. As shown by Yuan and Hamilton (1994), the use of a scaled hyperviscosity in the shallow-water system does not lead to convergence of the spectra and, in particular, the gravity wave component of the flow does not converge well with improvements in resolution.

The present analysis reveals another difficulty involved in formulating horizontal subgrid-scale parameterizations for GCMs, namely, the nature of the KE inputs. The standard picture is that KE is input largely through potential energy conversions at synoptic scales. The present analysis shows that even in the mid–lower troposphere, the potential energy conversions are significant over a broad range of wavenumbers for the model considered here. Thus, parameterizations based on the notion of a large-scale source forcing a downscale enstrophy cascade that is dissipated at small scales may not be entirely appropriate, although they may work well in practice. This becomes even more of a concern in the upper troposphere and middle atmosphere, where the eddy KE is largely generated by a flux of waves from below, and the resolved nonlinear triad (advective) interactions appear to play a fairly minor role in the KE budget.

The results from this study come with a number of caveats. The evidence of nonconvergence of the model spectra and aspects of the spectral KE budget as model resolution is improved supports the conclusion that the current subgrid-scale parameterizations may be inadequate, but also raises questions about the realism of the simulations themselves. The present conclusion about the maintenance of the mesoscale spectral regime must also be qualified by a recognition that the model does not explicitly represent the convective forcing scales, but relies on a crude convective parameterization acting on the model grid scale. By contrast, the regional-scale model of Vallis et al. (1997), which showed the possibility of an upscale cascade from convective energy input, had a horizontal grid spacing of 1 km. The robustness of the present results to still further increases in model resolution and to changes in modeled physical processes certainly requires further attention as computer resources allow.

The present study has been limited to July simulations. The 2D KE spectra have also been computed for the SKYHI N90L40 model from a January simulation. These results have been reported in Koshyk et al. (1999a) and show almost no seasonal variation in the spectrum, except at the very largest scales. Koshyk et al. also show spectra computed from several other GCMs (with more modest horizontal resolution). None of the models display a significant seasonal cycle of the KE spectrum outside of the largest scales. Furthermore, the spectral KE budget computed for the N90L40 model from the January simulation (not shown) is very similar to the corresponding July results shown here.

Research is continuing on the thermodynamic processes in the SKYHI model and on the available potential energy budget. Another area of interest involves the budgets of passive tracers in the middle atmosphere and the roles played by horizontal and vertical mixing processes at high horizontal and vertical resolution.

Acknowledgments. The authors are grateful to Jerry Mahlman for discussions contributing to the development of the diagnostic framework used here and for his interest and support throughout this project. The authors also acknowledge his efforts over the years to develop a global model with explicit representation of high-frequency motions. Interactions with Ted Shepherd have proven extremely useful and illuminating for physically interpreting many of the results presented here. The assistance of Richard Hemler in conducting the high-resolution SKYHI integrations is appreciated. The UKMO assimilated data used in the study were generously provided by the British Atmospheric Data Centre (BADC). Comments on the manuscript by Paul Kushner, Jerry Mahlman, Ted Shepherd, and three anonymous referees are gratefully acknowledged.

APPENDIX

Expressions for the Kinetic Energy Spectrum

The two expressions for the KE spectrum given in (3) and (5) are summed over the zonal index m to produce the results in Fig. A1. The spectra represent monthly mean values for a single July simulation using the N270L40 model described in section 2. Vertically averaged values over the 92–353-mb layer are shown. The spectra differ significantly for $n \lesssim 10$ and are essentially identical for $n \gtrsim 10$.

In plane geometry, it is easy to show that

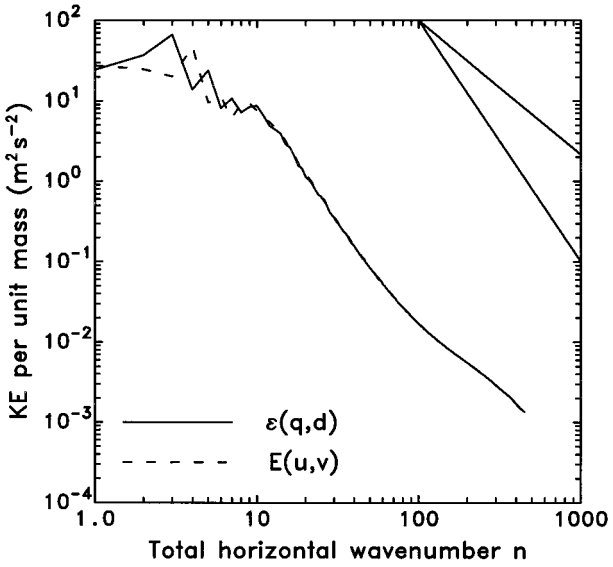

FIG. A1. N270L40 Jul mean KE spectra for the 92–353-mb layer. The spectra obtained from two different expressions are shown. The expressions for $E(u, v)$ and $\mathcal{E}(q, d)$ are obtained from (3) and (5), respectively, after summing each over the zonal index m.

$$E_{k,l}(p, t) = \frac{1}{4}(|u_{k,l}(p, t)|^2 + |v_{k,l}(p, t)|^2)$$
$$= \frac{1}{4}\frac{(|\zeta_{k,l}(p, t)|^2 + |\delta_{k,l}(p, t)|^2)}{(k^2 + l^2)}$$
$$= \mathcal{E}_{k,l}(p, t), \quad \text{(A1)}$$

where (k, l) are wavenumbers in the x and y directions, respectively,

$$u(x, y, p, t) = \sum_{k=0}^{K}\sum_{l=0}^{L} u_{k,l}(p, t)e^{ikx}e^{ily}$$
$$v(x, y, p, t) = \sum_{k=0}^{K}\sum_{l=0}^{L} v_{k,l}(p, t)e^{ikx}e^{ily}, \quad \text{and} \quad \text{(A2)}$$
$$\zeta(x, y, p, t) = \frac{\partial v}{\partial x} - \frac{\partial u}{\partial y}$$
$$\delta(x, y, p, t) = \frac{\partial u}{\partial x} + \frac{\partial v}{\partial y}, \quad \text{(A3)}$$

so that the expressions for $E_{k,l}$ and $\mathcal{E}_{k,l}$ are identical. This equivalence results from the fact that the complex exponential basis functions in (A2) are eigenfunctions of the operators $\partial/\partial x$ and $\partial/\partial y$. Thus, a given vortical or divergent mode with wavenumbers (k, l) depends only on the velocity field at exactly the same scale.

In spherical geometry, the expressions for vorticity and divergence are given by

$$\zeta(\lambda, \phi, p, t) = \frac{1}{a\cos\phi}\left[\frac{\partial v}{\partial \lambda} - \frac{\partial(u\cos\phi)}{\partial\phi}\right]$$
$$\delta(\lambda, \phi, p, t) = \frac{1}{a\cos\phi}\left[\frac{\partial u}{\partial \lambda} + \frac{\partial(v\cos\phi)}{\partial\phi}\right], \quad \text{(A4)}$$

where the velocities are defined in (2). Applying the derivatives in (A4) to the spherical harmonics shows that a given vortical or divergent mode with scale (m, n) depends on velocities at scales $(m, n - 1)$ and $(m, n + 1)$, because the Legendre polynomials in (2) are *not* eigenfunctions of the operator $\partial(\cos\phi\ )/\partial\phi$. This explains why the two curves in Fig. A1 are ''out of phase'' with one another at large scales. At smaller scales the effect is evidently much less pronounced.

Thus, when the streamfunction and velocity potential rather than u and v are expanded in spherical harmonic series, and the global mean quantity $\frac{1}{2}\langle \mathbf{v} \cdot \mathbf{v} \rangle$ is computed [where $\mathbf{v}$ is given in (4)], the expression (5) is obtained for the KE spectrum.

REFERENCES

Andrews, D. G., J. D. Mahlman, and R. W. Sinclair, 1983: Eliassen-Palm diagnostics of wave–mean flow interactions in the GFDL SKYHI general circulation model. *J. Atmos. Sci.,* **40,** 2768–2784.

Baer, F., 1972: An alternate scale representation of atmospheric energy spectra. *J. Atmos. Sci.,* **29,** 649–644.

Bartello, P., 1995: Geostrophic adjustment and inverse cascades in rotating stratified turbulence. *J. Atmos. Sci.,* **52,** 4410–4428.

Boer, G. J., 1983: Homogeneous and isotropic turbulence on the sphere. *J. Atmos. Sci.,* **40,** 154–163.

——, 1994: Mean and transient spectral energy and enstrophy budgets. *J. Atmos. Sci.,* **51,** 1765–1779.

——, and T. G. Shepherd, 1983: Large-scale two-dimensional turbulence in the atmosphere. *J. Atmos. Sci.,* **40,** 164–184.

——, N. A. McFarlane, and R. Laprise, 1984: The climatology of the Canadian Climate Centre general circulation model as obtained from a 5-year simulation. *Atmos.–Ocean,* **22,** 430–473.

Charney, J. G., 1947: The dynamics of long waves in a baroclinic westerly current. *J. Meteor.,* **4,** 135–162.

——, 1971: Geostrophic turbulence. *J. Atmos. Sci.,* **28,** 1087–1095.

——, and P. G. Drazin, 1961: Propagation of planetary-scale disturbances from the lower into the upper atmosphere. *J. Geophys. Res.,* **66,** 83–109.

Cho, J. Y. N., R. E. Newell, and J. D. Barrick, 1999a: Horizontal wavenumber spectra of winds, temperature, and trace gases during the Pacific Exploratory Missions: 2. Gravity waves, quasi-two-dimensional turbulence, and vortical modes. *J. Geophys. Res.,* **104,** 16 297–16 308.

——, and Coauthors, 1999b: Horizontal wavenumber spectra of winds, temperature, and trace gases during the Pacific Exploratory Missions: 1. Climatology. *J. Geophys. Res.,* **104,** 5697–5716.

Farge, M., and R. Sadourny, 1989: Wave-vortex dynamics in rotating shallow water. *J. Fluid Mech.,* **206,** 443–462.

Fels, S. B., J. D. Mahlman, M. D. Schwarzkopf, and R. W. Sinclair, 1980: Stratospheric sensitivity to perturbations of ozone and carbon dioxide: Radiative and dynamical response. *J. Atmos. Sci.,* **37,** 2265–2297.

Fjørtoft, R., 1953: On the changes in the spectral distribution of kinetic energy for two-dimensional non-divergent flow. *Tellus,* **5,** 225–230.

Fritts, D. C., R. C. Blanchard, and L. Coy, 1989: Gravity wave struc-

ture between 60 and 90 km inferred from space shuttle reentry data. *J. Atmos. Sci.,* **46,** 423–434.

Gage, K. S., and G. D. Nastrom, 1986: Theoretical interpretation of atmospheric wavenumber spectra of wind and temperature observed by commercial aircraft during GASP. *J. Atmos. Sci.,* **43,** 729–740.

Hamilton, K., 1993: What we can learn from general circulation models about the spectrum of middle atmospheric motions. *Coupling Processes in the Lower and Middle Atmosphere,* E. V. Thrane, T. A. Blix, and D. C. Fritts, Eds., Kluwer Academic, 161–174.

——, and J. D. Mahlman, 1988: General circulation model simulation of the semiannual oscillation of the tropical middle atmosphere. *J. Atmos. Sci.,* **45,** 3212–3235.

——, R. J. Wilson, J. D. Mahlman, and L. J. Umscheid, 1995: Climatology of the SKYHI troposphere–stratosphere–mesosphere general circulation model. *J. Atmos. Sci.,* **52,** 5–43.

——, ——, and R. S. Hemler, 1999: Climatology of the middle atmosphere simulated with high vertical and horizontal resolution versions of a general circulation model: Improvements in the cold pole bias and generation of a QBO-like oscillation in the tropics. *J. Atmos. Sci.,* **56,** 3829–3846.

Hayashi, Y., D. G. Colder, J. D. Mahlman, and S. Miyahara, 1989: The effect of horizontal resolution on gravity waves simulated by the GFDL SKYHI general circulation model. *Pure Appl. Geophys.,* **130,** 421–443.

Hines, C. O., 1960: Internal atmospheric gravity waves at ionospheric heights. *Can. J. Phys.,* **38,** 1441–1481.

Jones, P. W., K. Hamilton, and R. J. Wilson, 1997: A very high resolution general circulation model simulation of the global circulation in austral winter. *J. Atmos. Sci.,* **54,** 1107–1116.

Kolmogorov, A. N., 1941: The local structure of turbulence in incompressible viscous fluid for very large Reynolds number. *Comptes Rendus Acad. Sci. URSS,* **30,** 301–305.

Koshyk, J. N., and G. J. Boer, 1995: Parameterization of dynamical subgrid-scale processes in a spectral GCM. *J. Atmos. Sci.,* **52,** 965–976.

——, B. A. Boville, K. Hamilton, E. Manzini, and K. Shibata, 1999a: The kinetic energy spectrum of horizontal motions in middle-atmosphere models. *J. Geophys. Res.,* **104,** 27 177–27 190.

——, K. Hamilton, and J. D. Mahlman, 1999b: Simulation of the $k^{-5/3}$ mesoscale spectral regime in the GFDL SKYHI general circulation model. *Geophys. Res. Lett.,* **26,** 843–846.

Kraichnan, R. H., 1967: Inertial ranges in two-dimensional turbulence. *Phys. Fluids,* **10,** 1417–1423.

Lambert, S. J., 1984: A global available potential energy-kinetic energy budget in terms of the two-dimensional wavenumber for the FGGE year. *Atmos.–Ocean,* **22,** 265–282.

Laursen, L., and E. Eliasen, 1989: On the effects of the damping mechanisms in an atmospheric general circulation model. *Tellus,* **41A,** 385–400.

Levy, H., J. D. Mahlman, and W. J. Moxim, 1982: Tropospheric N_2O variability. *J. Geophys. Res.,* **87,** 3061–3080.

Lilly, D. K., 1969: Numerical simulation of two-dimensional turbulence. *Phys. Fluids Suppl. II,* **12,** 240–249.

——, 1983: Stratified turbulence and the mesoscale variability of the atmosphere. *J. Atmos. Sci.,* **40,** 749–761.

Lorenz, E. N., 1967: The nature and theory of the general circulation of the atmosphere. World Meteorological Organization Report, Publication Number 218, 161 pp.

Manzini, E., and K. Hamilton, 1993: Middle atmosphere traveling waves forced by latent and convective heating. *J. Atmos. Sci.,* **50,** 2180–2200.

Nastrom, G. D., and K. S. Gage, 1985: A climatology of atmospheric wavenumber spectra of wind and temperature observed by commercial aircraft. *J. Atmos. Sci.,* **42,** 950–960.

——, ——, and W. H. Jasperson, 1984: Kinetic energy spectrum of large- and mesoscale atmospheric processes. *Nature,* **310,** 36–38.

O'Neill, A., and V. D. Pope, 1988: Simulations of linear and nonlinear disturbances in the stratosphere. *Quart. J. Roy. Meteor. Soc.,* **114,** 1063–1110.

Polvani, L. M., J. C. McWilliams, M. A. Spall, and R. Ford, 1994: The coherent structures of shallow-water turbulence: Deformation radius effects, cyclone/anticyclone asymmetry and gravity-wave generation. *Chaos,* **4,** 177–186.

Saltzman, B., and S. Teweles, 1964: Further statistics on the exchange of kinetic energy between harmonic components of the atmospehric flow. *Tellus,* **16,** 432–435.

Scinocca, J. F., and P. H. Haynes, 1998: Dynamical forcing of stratospheric planetary waves by tropospheric baroclinic eddies. *J. Atmos. Sci.,* **55,** 2361–2392.

Smagorinsky, J., 1953: The dynamical influence of large-scale heat sources and sinks on the quasi-stationary mean motions of the atmosphere. *Quart. J. Roy. Meteor. Soc.,* **79,** 342–366.

——, 1963: General circulation experiments with the primitive equations. I. The basic experiment. *Mon. Wea. Rev.,* **91,** 99–164.

——, S. Manabe, and J. L. Holloway Jr. 1965: Numerical results from a nine-level general circulation model of the atmosphere. *Mon. Wea. Rev.,* **93,** 727–768.

Strahan, S. E., and J. D. Mahlman, 1994a: Evaluation of the SKYHI general circulation model using aircraft N2O measurements 1. Polar winter stratospheric meteorology and tracer morphology. *J. Geophys. Res.,* **99,** 10 305–10 318.

——, and ——, 1994b: Evaluation of the SKYHI general circulation model using aircraft N2O measurements 2. Tracer variability and diabatic meridional circulation. *J. Geophys. Res.,* **99,** 10 319–10 332.

Swinbank, R., and A. O'Neill, 1994: A stratosphere–troposphere data assimilation system. *Mon. Wea. Rev.,* **122,** 686–702.

Tang, C.-M., and S. A. Orszag, 1978: Two-dimensional turbulence on the surface of a sphere. *J. Fluid Mech.,* **872,** 305–318.

Vallis, G. K., G. J. Shutts, and M. E. B. Gray, 1997: Balanced mesoscale motion and stratified turbulence forced by convection. *Quart. J. Roy. Meteor. Soc.,* **123,** 1621–1652.

VanZandt, T. E., 1982: A universal spectrum of buoyancy waves in the atmosphere. *Geophys. Res. Lett.,* **9,** 575–578.

Yuan, L., and K. Hamilton, 1994: Equilibrium dynamics in a forced-dissipative f-plane shallow water model. *J. Fluid Mech.,* **280,** 369–394.